

Photonics Letters of Poland



Peer reviewed journal of the
Photonics Society of Poland

Vol 13, No 4
2021

ISSN: 2080-2242



Special issue co-sponsored by
Warsaw University of Technology

**Warsaw University
of Technology**



Holographic anniversaries: a tribute to holographic pioneers

Małgorzata Kujawińska

Faculty of Mechatronics, Warsaw University of Technology, Św. Andrzeja Boboli 8, 02-525 Warszawa, Poland

Received December 29, 2021; accepted December 30, 2021; published December 31, 2021

Abstract—This editorial presents shortly the holographic timeline and the most important holographic pioneers. This is the background to an overview of the contents of this special issue of the Photonics Letters of Poland, devoted mainly to digital holography. The published papers from international research groups present a wide range of approaches and applications, including metrology, displays, computer-generated holograms, and biomedicine.

This special issue of Photonics Letters of Poland is a tribute to the pioneers of holography (Fig.1) and the celebration of three significant anniversaries. **Hundred years ago (in 1920)**, Polish scientist **Mieczysław Wolfke** published in *Physikalische Zeitschrift* the paper in which he proposed theoretically the concept of holography based on optical imaging theory. Wolfke's works were unfortunately forgotten for many years. After **Dennis Gabor's** paper in 1948, in which he presented theoretically and experimentally the concept of holography and which led him to receiving **fifty years ago a Nobel Prize (in 1971)**, several important inventions which happened in the 1960s.

Sixty years ago, in 1962, **Yuri Nikolaevich Denisyuk** and **Emmett Leith & Juris Upatnieks** published their seminal papers on reflection holography and off-axis holography, respectively. Together with the invention of the laser (in 1960), these works had a substantial impact on making holography a much more practical and popular discipline. During the late sixties, **Stephen Benton** proposed rainbow holograms opening up the science of holography to artists and security applications. At the same time, **Adolf Lohmann** introduced computer-generated holograms where computers were used to numerically generate holograms to be printed and photographed for optical reconstruction. Finally, **Joseph W. Goodman** and **Leonid Yaroslavsky** proposed using an electronic recording of holograms, followed by numerical processing to reconstruct the object digitally. This invention had opened a new era of holography, namely digital holography.

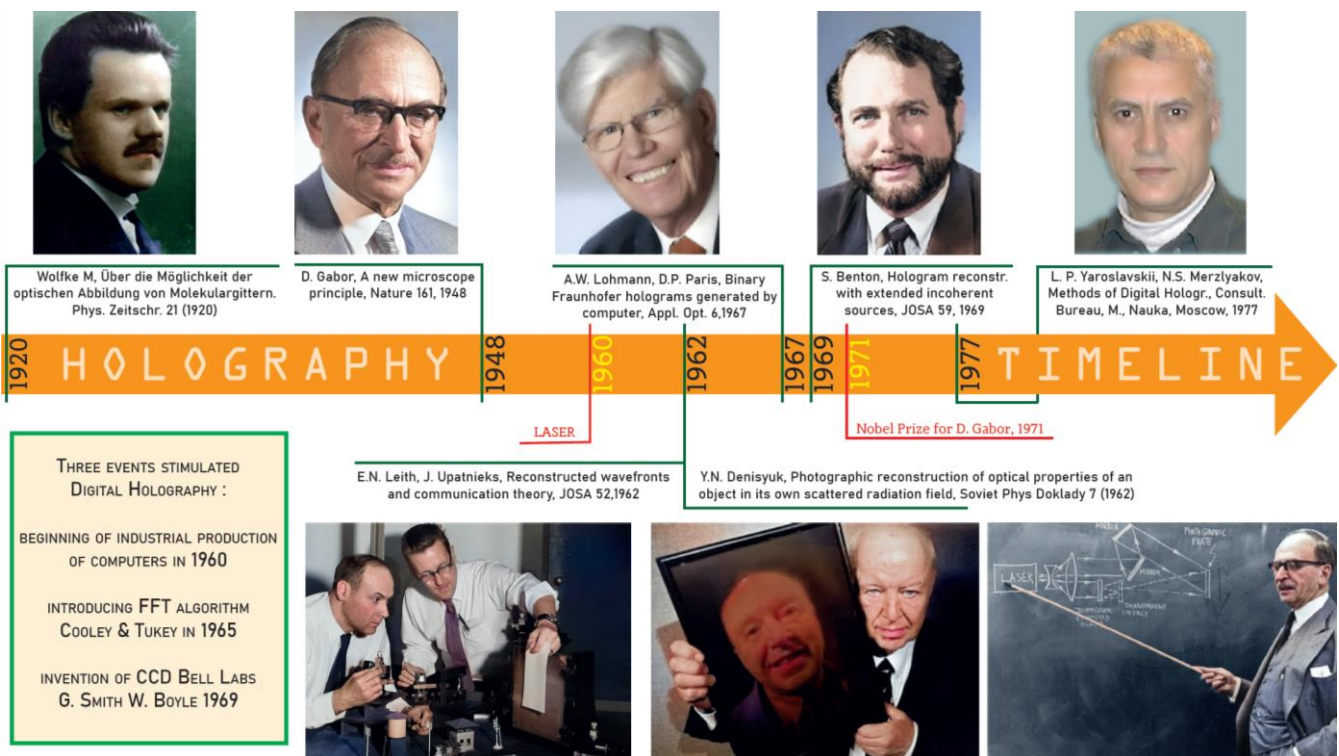


Fig. 1. Holography timeline: from optical to digital holography.

This special issue starts with the paper by Krzysztof Petelczyc, which describes the history of Wolfke's pioneering work on holography and tries to recreate the thought process that led to it. It is worth reminding that Dennis Gabor mentioned Mieczysław Wolfke as the person who proposed the principles of holography as early as 1920 (which Gabor did not know, independently making the same discovery).

The following papers are focused on various aspects and applications of digital holography and computer-generated holograms.

Ichirou Yamaguchi, the inventor of phase-shifting digital holography, reminds the readers of the principles and importance of this technique and introduces its further improvements applied to shape and deformation measurements.

Pascal Picard discusses recent advances in speckle decorrelation noise removal from phase data delivered by holographic interferometry. Two main topics are considered: modeling the decorrelation noise in digital Fresnel holography and a new approach to speckle denoising using deep convolution neural networks.

Weijie Wu, Mike Pivnenko, and Daping Chu provide an overview of the applications of phase-only LCOS in two-dimensional (2D) digital holography, including the fundamental operating principle of phase-only LCOS SLMs and their hardware performance. They also discuss LCOSes potential improvements and applications for futuristic holographic displays.

The paper by Jędrzej Szpygiel, Maksymilian Chlipała, Rafał Kukołowicz, Moncy Idicula, and Tomasz Kozacki presents a distortion correction method enabling a distortion minimized, large size image in a wide-angle holographic projector, which is highly demanded by the display market. This technique applies numerical predistortion of an input image used for hologram generation. It is based on the estimation of distortion coefficients by comparing optically a reconstructed point test chart with its original.

The subsequent three papers are devoted to an improvement of computer hologram generation methods with specific functionalities. The joint paper by Michał Makowski and Tomoyoshi Shimobaba addresses the problem of limited efficiency of random-phase free computer-generated holograms in the case of high contrast binary images with dominant high spatial frequencies.

The paper by Mateusz Sadowski and Michał Makowski describes numerical optimization of the process of writing and reconstructing 2-D images in binary-phase computer-generated holograms stored in binary photo-magnetic materials. Such materials showed efficient and ultra-fast rewriting of holograms where the intensity of threshold allows for a dense, sub-diffraction limit packing of hologram points.

Mateusz Surma, Mateusz Kałuża, Patrycja Czerwińska, Paweł Komorowski, and Agnieszka Siemion present a new approach to designing diffractive optical elements (CGH) for THz radiation. The design utilizes a neural network-based algorithm, which can address the problem of small f-number values and is also suitable for complicated distributions.

Finally, the outstanding role of digital holographic microscopy in biomedical applications at cellular level is addressed in the paper by Arkadiusz Kuś, Wojciech Krauze, and Małgorzata Kujawińska. They present the history and outlook on the development of optical diffraction tomography with holographic projections and optical coherence tomography, two seemingly distant techniques that have recently been brought close together by a common theoretical model described by the common k-space theory. With this common ground, the authors expect a multitude of exciting new holography-tomography systems to appear in the next few years.

The presented papers are just a small sample of a great number of research works and commercial efforts related to holography field. With constant progress in novel materials, detectors, spatial light modulators, integrated photonics and computer power it is expected that holography, being the most versatile imaging and measurement method, will finally take the rightful place in multiple areas of our life.

Mieczysław Wolfke - a pioneer of holography

Krzysztof Petelczyc*

Faculty of Physics, Warsaw University of Technology, Koszykowa 75, 00-662 Warszawa, POLAND

Received July 28, 2021; accepted September 11, 2021; published December 31, 2021

Abstract—Receiving the Nobel Prize in 1971 for the invention and development of the holographic method, Dennis Gabor mentioned Mieczysław Wolfke as the person who proposed this method as early as 1920 (which he did not know, independently making the same discovery). This article describes the history of Wolfke's pioneering work and tries to recreate the thought process that led to it - starting with the task of supplementing and verifying the diffraction grating theory proposed by Ernst Abbe, which he carried out as part of his doctorate at the University of Wrocław and habilitation at the University of Zurich and the Swiss Federal Institute of Technology in Zurich.

According to the recollections of Witold Łaniecki, a student and collaborator of Mieczysław Wolfke, his mentor valued the doctorate on the resolving power of diffraction gratings and the article from 1920 on imaging molecular grids as his own most significant achievements [1]. Such a statement is surprising, while the result of his work was also the method that allowed Willem Keesom to solidify helium for the first time [2] and their joint discovery of two types of liquid helium [3]. Even during Wolfke's lifetime, these achievements were widely echoed in the scientific world. This cannot be said about his achievements in optics [4], which were appreciated after half a century.

When Ernst Abbe, the optician who revolutionized the theory of imaging and the construction of optical systems, died in 1905, many of his achievements were not entirely written and published. The well-known scientist often presented his theories in the form of lectures and seminars. Their listener was, among others, Otto Lummer, a German physicist who played an essential role in the formation of quantum theory. In 1904 Lummer became a professor of physics at the University of Wrocław (at that time in Germany). In the face of Abbe's death, he made it a point of honor to write down the master's achievements in a complete and synthetic form. The culmination of this project was the book *Die Lehre von der Bildentstehung im Microscope* published in 1910 [5].

In the development of Abbe's theory, Lummer was supported by two younger collaborators - Mieczysław Wolfke and Fritz Reiche. The latter, just after a doctorate in Berlin from Max Planck, applied for a job at the University of Wrocław. On the other hand, Wolfke came to Wrocław for further studies (initially concerning the

influence of X-rays on radium) from the University of Paris. Both were characterized by the research abilities necessary to analyze and develop the mathematical equations and diffraction integrals used by Abbe [6, 7].



Fig. 1. Fritz Reiche and Otto Lummer, ca. 1910 (coloured).



Fig. 2. Mieczysław Wolfke with his wife Agnes Erica, ca. 1912.

Reiche's work concerned the reconciliation of Abbe's theory with the modern theories of Kirchhoff and Maxwell. At the same time, Wolfke's doctorate verified compliance with the experiment of the theory of diffraction gratings imaging in a microscope with a diaphragm placed in the focal plane. The problem that we call today spatial filtration was meticulously derived theoretically and elaborated [8]. One conclusion was that no matter how obscured, the image is always symmetrical. Unfortunately, this conclusion did not agree with the results of the experiments, where for asymmetrical diaphragms, an asymmetrical image was also created. As Wolfke wrote: "the reason for this asymmetry of the image lies in the greater or lesser

* E-mail: krzysztof.petelczyc@pw.edu.pl

transparency of the mesh bars" (in the original source: *przyczyna tej asymetrii obrazu leży w większej lub mniejszej przezroczystości sztab siatki*) [9]. After defending his doctorate, he developed this problem, supplementing and generalizing his theory into gratings with a non-binary transmittance profile and obtaining full compliance with the experiment [10-12]. The development of this topic was possible thanks to his employment in the scientific laboratories of the Carl-Zeiss Optical Plant in Jena - the same of which the "founding father" was Ernst Abbe. There, thanks to the support of the head of microscopy department, August Köhler, he obtained over sixty different diffraction gratings for examination - elements that were expensive and inaccessible at the time. It turned out that the silvering technique did not allow to obtain full opacity, and the less light the lattice bars let through, the better the diffraction pattern corresponded to the theory [13].

Working in the optics industry did not match Wolfke's ambitions. Therefore, he was looking for employment at university. Unfortunately, no position was created for him at the University of Wrocław, but in 1912 Wolfke got employed as an assistant to the "father of liquid crystals," prof. Otto Lehmann at the Karlsruhe Institute of Technology [13]. Hence the research area of the team focused on studying the crystalline structure of materials. This context was crucial in Wolfke's pioneering work in 1920, in which he treated atomic lattice as spatial diffraction grating. It is worth noting that these considerations were conducted while Paul Peter Ewald and Max von Laue published the world's first papers containing such an approach, and a year later, William Henry Bragg, with his son William Lawrence invented X-ray diffraction [14]. They could inspire Wolfke in his research work. A year's work in Karlsruhe and experience in the physics of crystal lattices gave him the necessary knowledge and skills both in the field of optics and quantum approach, which was the subject of intensive work on redefining the concept of atoms and the structure of radiation.

Wolfke's dream was habilitation and the related *veniam legendi* (the right to lecture) at a leading European university. The achievement of this goal required summarizing and completing research on Abbe's theory. An unresolved issue was the generalization of the diffraction integrals to the incoherent light case where Abbe's equations did not correctly describe the experimental results. According to the terminology of the time, they concerned self-illuminating objects, i.e., extended light sources, and non-self-illuminating ones, i.e., slides illuminated by light transmitted through a pinhole or a slit. As Wolfke wrote, "the purpose of this work is to derive general equations for optical images of

self-illuminating and non-illuminating objects using one and the same method, regardless of the object's position in relation to the set plane." (In the original source: *celem pracy niniejszej jest wyprowadzenie równań ogólnych dla obrazów optycznych przedmiotów samoświecących i niesamoświecących jedną i tą samą metodą, i to niezależnie od położenia przedmiotu w stosunku do płaszczyzny nastawienia.*) [15] Starting from the Huygens-Fresnel principle and applying the Lambert cosine law for the angles of incidence of light, he derived a theoretical model that correctly described the experimental results for both types of lighting [16] and generalized it to different positions of the input plane [17].

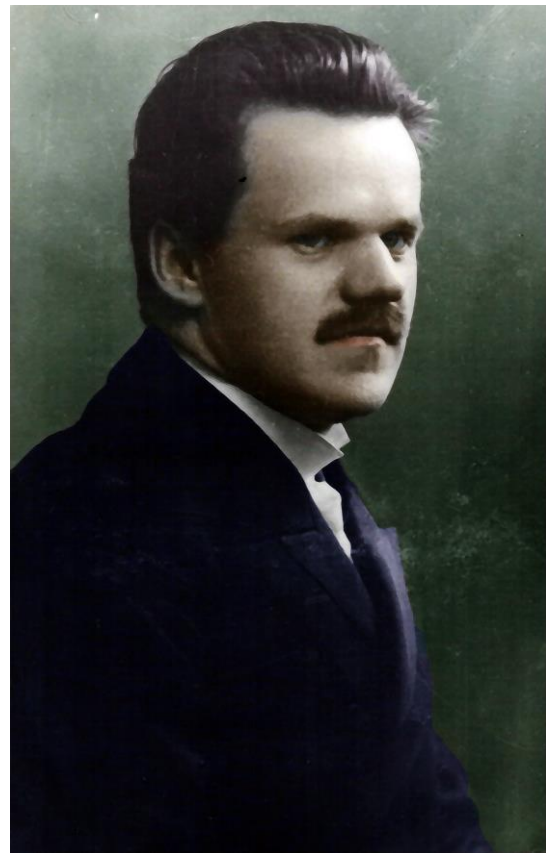


Fig. 3. Mieczysław Wolfke, 1915.

The developed theory became the basis for the habilitation in 1913 at the Swiss Federal Institute of Technology in Zurich, where Albert Einstein and Pierre Weiss reviewed Wolfke's achievements, and a year later at the University of Zurich with a favorable opinion of Max von Laue and Alfred Kleiner [13]. Wolfke settled in Switzerland, where he participated in meetings of scientists setting world trends in modern physics. He also published various models interpreting Einstein's light quanta and suggesting the concept of light molecules as possible excitation states of the cavity [18-21].

Meanwhile, the First World War was taking place in Europe, which changed the map of the continent. The most important result of the new geopolitical situation for Wolfke was the revival of his homeland - Poland, which disappeared from the maps of Europe, divided between Russia, Prussia, and Austria at the end of the 18th century. In 1920, Wolfke was offered the Chair of Theoretical Physics at the University of Warsaw. He resigned from work at both universities in Zurich, but the transfer to Poland eventually did not occur due to financial problems. Returning to the academic community in Zurich required repeating the habilitation procedure in 1921 (Edgar Meyer and Erwin Schrödinger were appointed reviewers). However, a year later, Wolfke was appointed professor at the Warsaw University of Technology with a promise to cover travel expenses and provide accommodation on the spot. In the review prepared for the competition for this position, the outstanding Polish physicist Stefan Pieńkowski analyzed Wolfke's scientific achievements, concluding that "the most serious achievements are the works (...) concerning light bending, made partly under the influence of the research of prof. Lummer; they constitute a certain unitary whole and give a clear solution to the question raised. The overall scientific activity of Dr. M. Wolfke shows a great scientific background, mastery of the newest directions of physics and easy mathematical approach to phenomena" (in the original source: *najpoważniejszy dorobek stanowią prace (...) dotyczące uginania światła, wykonane częściowo pod wpływem badań prof. Lummera; stanowią one pewną jednolitą całość i dają wyraźne rozwiązanie postawionej kwestii. Całokształt działalności naukowej P. Dr. M. Wolfkego wykazuje wielkie wyrobienie naukowe, opanowanie najnowszych kierunków fizyki i łatwość matematycznego ujęcia zjawisk.*) [22].



Fig. 4. Weesen, Switzerland, 1922.

Under these circumstances, most likely in the Hotel du Lac in Weesen, where Wolfke was preparing for his would-be move to Poland, a paper was created, which

was first in the world to consider the concept of holography. The article published in *Physikalische Zeitschrift* is dated "April 1920" [23]. It was the culmination of optical imaging theory and expression of a concept that the author himself probably considered extremely brave. Indeed, before deciding to publish it, he was also looking for the possibility of experimentally verifying his considerations. Today we know that he had no chance of obtaining high-quality results due to the lack of strong, coherent light sources (the laser was not constructed until the year 1960). Therefore, Dennis Gabor was able to say in 1971, when receiving the Nobel Prize for the invention and development of the holographic method, that "Wolfke had proposed this method in 1920, but without realizing it experimentally" [24].

As the aim of the work Wolfke set himself was "a more detailed study of the possibilities of optical imaging of molecular structures" (in the original source: *die Möglichkeit einer optischen Abbildung von molekularen Gebilden näher untersuchen*) [23]. Then he stated that it is impossible to visualize the atomic structure classically because to achieve the necessary resolution, very short (X-ray) waves would have to be used, resulting in significant diffraction effects. Therefore, only the diffraction field image, called the primary image, is recordable. The reconstruction of the secondary image, geometrically similar to the imaged crystal lattice, faces the lack of optical elements working for such short wavelengths. Wolfke proposed to record the original image and then use visible light in the second part of the process after developing the film. He was aware that in order for this process to be successful, the subject had to meet specific additional requirements. He put it in the following theorem: "In monochromatic, parallel, orthogonal illumination, the diffraction image of a diffraction image of a symmetrical object without a phase structure will be identical to that object." (in the original source: *Bei monochromatischer, paralleler, senkrechter Beleuchtung ist das Beugungsbild eines Beugungsbildes eines symmetrischen Objektes ohne Phasenstruktur identisch mit dem Abbild dieses Objektes*) [23] Then the author proves this theorem starting from the general equation of the optical imaging theory he developed [16] and confirms that he has verified its validity experimentally using various optical gratings and a parallel sodium light beam. However, he does not include the obtained images, stating that "to obtain a sharp image in these experiments, it was necessary to use very strong light beams and very small collimation holes" (in the original source: *Bei diesen Versuchen muß, um scharfe Bilder zu erhalten, eine möglichst starke Lichtquelle mit sehr kleinem punktförmigen Kollimatorschlitz benutzen werden*) [23].

Über die Möglichkeit der optischen Abbildung von Molekulargittern).
Von M. Wolfke.

Wir wollen hier die Möglichkeit einer optischen Abbildung von molekularen Gebilden näher untersuchen.

Eine direkte Abbildung einer molekularen Struktur mit irgendeiner Strahlenart ist undenkbar, und zwar aus folgendem Grunde: Die zur Abbildung notwendige Wellenlänge müßte so klein sein, daß ihr gegenüber eine Anhäufung von Molekülen, z. B. ein Kristallgitter, nicht als ein Kontinuum erscheinen, sondern jedes Molekül für sich ein Beugungsbild erzeugen würde. Nur dann kann das Beugungsbild, das sogenannte primäre oder Zwischenbild, entstehen. Ist aber die Wellenlänge genügend klein, so wird die Entstehung eines Abbildes, d. h. des sekundären Interferenzbildes ausgeschlossen sein, da dann auch die Linsen und die Spiegel nicht mehr als Kontinua dieser Wellenlänge gegenüber erscheinen und eine Brechung oder Reflexion im gewöhnlichem Sinne nicht zustande kommen kann.

Es ist aber denkbar, den Abbildungsvorgang, den man theoretisch stets in zwei Stadien trennt, auch praktisch zu trennen und die Erzeugung des primären Bildes z. B. den Röntgenstrahlen zu überlassen und das sekundäre Bild mit sicht-

$$I_1 = \text{const.} \left\{ \iint_{\text{Objekt}} dX dY \varphi(X, Y) \cdot \sqrt{\cos(\varepsilon - u_0)} \cdot \cos 2\pi \left[\varphi(X, Y) - \frac{\beta X + \gamma Y}{\lambda} - \frac{n}{n'} \frac{\xi X + \eta Y}{\lambda} \right]^2 + \right. \\ \left. + \text{const.} \left\{ \iint_{\text{Objekt}} dX dY \varphi(X, Y) \cdot \sqrt{\cos(\varepsilon - u_0)} \cdot \sin 2\pi \left[\varphi(X, Y) - \frac{\beta X + \gamma Y}{\lambda} - \frac{n}{n'} \frac{\xi X + \eta Y}{\lambda} \right]^2 \right\} \right\} \quad (1)$$

bares Licht zu erzeugen, indem man in einem optischen Abbildungssystem das primäre Bild durch das mittels Röntgenstrahlen photographisch aufgenommene Beugungsbild ersetzt. Allerdings kann dieses Verfahren nicht in allen beliebigen Fällen ein ähnliches Abbild liefern, da die Photographie des Beugungsbildes nur seine Intensitätsverteilung, d. h. die Amplituden wiedergibt, nicht aber die Phasenverteilung, die bei der Entstehung des Abbildes im allgemeinen ebenfalls eine maßgebende Rolle spielt.

Die nähere Untersuchung dieser Frage führte mich zu einem neuen Satz der Abbildungstheorie, der die Realisierung einer optischen Abbildung von Molekulargittern prinzipiell ermöglicht. Dieser Satz lautet:

Bei monochromatischer, paralleler, senkrechter Beleuchtung ist das Beugungsbild eines Beugungsgitters eines symmetrischen Objektes ohne Phasenstruktur identisch mit dem Abbild dieses Objektes.

Um diesen Satz zu beweisen, knüpfen wir an die allgemeinen Gleichungen der Abbildungstheorie an¹⁾.

Bei einer punktförmigen Lichtquelle ist die Intensitätsverteilung im Beugungsbild (Zwischenbild) durch folgenden Ausdruck gegeben²⁾:

Objekt und $\sqrt{\cos(\varepsilon - u_0)}$ den Schwächungsfaktor nach dem Lambert'schen Gesetz.

Für paralleles Licht senkrecht zur Objektebene ist $\beta = \gamma = 0$ und $\phi = \psi = 0$. Findet die Abbildung in der Luft bei kleinen Öffnungswinkeln statt, so ist:

$$n = n' = 1 \text{ und } \sqrt{\cos(\varepsilon - u_0)} = 1.$$

Außerdem kann man bei Objekten ohne ausgeprägte Phasenstruktur $\varphi(X, Y) = \text{const.} = 1$ setzen und der Ausdruck (1) geht in, den folgenden über:

$$I_1 = \text{const.} \left\{ \iint_{\text{Objekt}} dX dY \varphi(X, Y) \cdot \cos 2\pi \left(\frac{\xi X + \eta Y}{\lambda} \right)^2 + \right. \\ \left. + \text{const.} \left\{ \iint_{\text{Objekt}} dX dY \varphi(X, Y) \cdot \sin 2\pi \left(\frac{\xi X + \eta Y}{\lambda} \right)^2 \right\} \right\} \quad (2)$$

1) Vergetragen in der Sitzung der Schweiz. Phys. Ges. in Zürich, am 24. April 1920.

2) M. Wolfke, Ann. d. Phys. (4), 30, 569, 1922, Habilitationsschr. Zürich 1924.

3) l. c., Formel (11a), S. 588.

References

- [1] W. Łaniecki, Kwartalnik Historii Nauki i Techniki, **21**, 545-553 (1976).
- [2] W. Keesom, Nature **118**, 81 (1926). doi: 10.1038/118081a0
- [3] W. Keesom, M. Wolfke, Konink. Akad. Wetensch. Amsterdam, Proc. **31**(190b), 90-94 (1928).
- [4] W. Keesom, *Helium* (Elsevier, Amsterdam 1942).
- [5] E. Abbe, *Die Lehre von der Bildentstehung im Mikroskop* (F. Vieweg, Braunschweig 1910).
- [6] R. Torge, Postępy Fizyki, **53**, 201-210 (2002).
- [7] A. Kiejna, Kwartalnik Historii Nauki i Techniki, **48**, 7 (2003).
- [8] M. Wolfke, Ann Phys. **339**, 277 (1911). doi: 10.1002/andp.19113392006
- [9] M. Wolfke, Prace matematyczno-fizyczne, **22**, 135 (1911).
- [10] M. Wolfke, Ann Phys. **342**, 96 (1912). doi: 10.1002/andp.19113420107
- [11] M. Wolfke, Ann Phys. **342**, 797 (1912). doi: 10.1002/andp.19123420409
- [12] M. Wolfke, Ann Phys. **343**, 385 (1912). doi: 10.1002/andp.19123430706
- [13] K. Petelczyc, E. Kędzierska, *Mieczysław Wolfke. Gdyby mi dali choć pół miliona...* (OWPW, Warszawa 2018).
- [14] L.A. Aslanov, G.V. Fetisov, J.A.K. Howard, "Crystallographic Instrumentation", Oxford (1998).
- [15] M. Wolfke, Wiadomości matematyczne **17**, 1 (1913).
- [16] M. Wolfke, Ann Phys. **344**, 569 (1912). doi: 10.1002/andp.19123441305
- [17] M. Wolfke, Ann Phys. **345**, 194 (1913). doi: 10.1002/andp.19133450108
- [18] M. Wolfke, Verhandlungen der DPG, **15**, 1123 (1913).
- [19] M. Wolfke, Verhandlungen der DPG, **15**, 1215 (1913).
- [20] M. Wolfke, Verhandlungen der DPG, **16**, 4 (1914).
- [21] M. Wolfke, Physikalische Zeitschrift, **22**, 375 (1921).
- [22] Akta osobowe – Wolfke Mieczysław, Archiwum Akt Nowych sygn. 2/14/0/6/6638, Warszawa
- [23] M. Wolfke, Physikalische Zeitschrift, **21**, 495 (1920).
- [24] S. Lundqvist, *Nobel Lectures, Physics 1971-1980* (World Scientific Publishing Co. Singapore 1992).

Fig. 5. First page of the original paper about the idea of holography from Physikalische Zeitschrift 21, 1920.

The conclusions of the work indicate the enlargement of the obtained image in a ratio of the reproducing and recording wavelengths, i.e., about 10,000 times, and the possibility of further optically magnifying the image up to 100 times. According to Wolfke, "this magnification is completely sufficient to visualize the molecular structure to obtain optical images of the crystal lattices." (in original source: *Diese Vergrößerung würde vollständig genügen, um die Molekularstruktur sichtbar zu machen*) The article concludes that the developed method allows for shifting the theoretical boundaries of optical imaging, which proves the awareness of the importance of this discovery for the history of physics. Unfortunately, at that time, optics was not technologically prepared for its implementation.

After arriving at the Warsaw University of Technology, Wolfke abandoned optical research to favor low-temperature and electro-physical field. After the Second World War, he returned to Zurich to restore contacts, obtain technical means to rebuild laboratories, and update the state of knowledge from the works that did not reach Poland during the war. In 1947, he died suddenly without receiving recognition for his achievements in the field of optics.

Shape and deformation measurements of rough surfaces by phase-shifting digital holography

Ichirou Yamaguchi

Scientist Emeritus of RIKEN, Higashi-Hisakata 3-4-32, Kiryu, Gunma 376-0053

Received November 14, 2021; accepted December 06, 2021; published December 31, 2021

Abstract—In digital holography recording the reconstruction of holograms is performed digitally by modern photonic devices to increase optical non-contacting measurements of various kinds of surfaces, both specular and rough. In this article we discuss these features of digital holography using phase shifting techniques that have greatly extended holographic capabilities.

Introducing a phase-shifting fringe pattern method of analysis into digital holography (DH) was an important step in its metrological applications. The basic setup for phase-shifting digital holography (PSDH) is modified by adding a PZT-mirror in the reference beam path as illustrated in Fig.1. The reference and object beam are travelling in the in-line configuration so the maximum bandwidth of object frequency can be captured. At least three holograms are acquired after stepwise phase shifts of the reference beam. The interference intensity detected by the CCD is given by:

$$I_H(x, y, \delta) = |U_R \exp(i\delta) + U(x, y)|^2 = |U_R|^2 + |U|^2 + 2\Re[U_R U^* \exp(i\delta)], \quad (1)$$

where U_R is the complex amplitude of the reference beam and δ is the phase difference between the object and the reference waves. By using the three phase-shifting procedure with a phase step of $\pi/2$, we can derive the complex amplitude of the object wave such as [1, 2]:

$$U(x, y) = \frac{1-i}{4U_R^*} \left\{ I_H(x, y, 0) - I_H(x, y, \frac{\pi}{2}) + i \left[I_H(x, y, \frac{\pi}{2}) - I_H(x, y, \pi) \right] \right\} \quad (2)$$

For analysis of image reconstruction, we adopt the coordinate system depicted in Fig. 2. The object wave at the CCD plane is represented as a Fresnel transform of the complex amplitude at the object plane $U(x, y)$ by:

$$U_i(X, Y, Z) = \iint U(x, y) \exp \left[ikZ + ik \frac{(X-x)^2 + (Y-y)^2}{2Z} \right] dx dy \quad (3)$$

where the integration is carried out over the area of CCD. We assume first a sufficient extension and ideal resolution of the device. Here the collimated reference beam is assumed with $z_R = \infty$. If we substitute Eq. (1) into Eq. (3),

we find that the image plane is determined from the condition that the quadratic term of x and y in the exponent vanishes such as $z = -z_o$, where the complex amplitude becomes:

$$U_i(X, Y, -z_o) = U_o(X, Y) \quad (4)$$

if we neglect the limitation of finite size of CCD array.

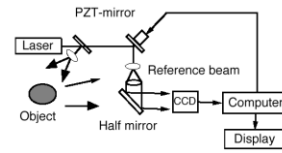


Fig. 1. Phase-shifting digital holography.

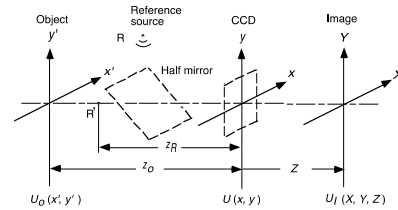


Fig. 2. Coordinate systems.

Image reconstruction (acc. Eq. (3)) can be numerically calculated by regarding it as either a Fourier transform or a convolution integral and replacing the integration by summation. In the first algorithm of reconstruction (the single FFT method), the sample interval of the image is given by $\lambda Z/L$, where L is the size of CCD. The second algorithm, which uses the double FFT method, keeps the sampling interval equal to be the pixel pitch of CCD independent of the reconstruction distance. If we record an object by using a geometry shown in Fig. 2, the resolution is given by $\Delta x = \lambda z_o/L$, while the focal depth of the reconstructed image is given by $\Delta z = \lambda(z_o/L)^2$. The maximum object size to be recorded is equal to $N\Delta x$ with the pixel number N along the x -direction in the single FFT algorithm, while it becomes equal to that of CCD in the double FFT method [3].

The phase to be detected by digital holography is given by the difference of the reconstructed complex amplitude that can be represented as follows [4]. The phase difference is due to changes of the incident angle or the wavelength of

an object illumination beam. The wave vectors of this beam are represented by k_a and k_b as shown in Fig. 3(a). If we denote the vectors representing the observation direction by k_{ao} and k_{bo} , the difference of the reconstructed phase corresponding to the identical points is given by:

$$\Phi(x, y) = \langle \arg(U_1) - \arg(U_2^*) \rangle = \frac{\langle U_1 U_2^* \rangle}{\sqrt{\langle I_1 I_2 \rangle}} = - (k_{az} - k_{bz} - k_{aoz} + k_{boz}) h(x, y) - (k_{az} - k_{bz}) x, \quad (5)$$

where the incident plane is in the x-z plane and the reference plane for the surface height is in the x-y plane. In Eq. (5) the first term on the right-hand side means the phase difference proportional to the surface height and the second term stands for tilt components.

If we change the wavelength of the illumination from λ_a to λ_b and reconstruct each of the hologram with the same wavelength as in hologram recording, the phase difference is expressed with the incident angle θ_s and normal observation by:

$$\Phi(x, y) = -(1 + \cos \theta_s)(k_a - k_b)h(x, y) = -2\pi(1 + \cos \theta_s)h(x, y) / \Lambda \quad (6)$$

which means the contours of an object height with a sensitivity that is associated with so called synthetic wavelength given by

$$\Lambda = 1 / (1/\lambda_a - 1/\lambda_b). \quad (7)$$

When the incident angle is changed from θ to $\theta + \Delta\theta$, the phase difference becomes:

$$\begin{aligned} \Phi(x, y) &= -k[\cos \theta - \cos(\theta + \Delta\theta)]h(x, y) - k[\sin \theta - \sin(\theta + \Delta\theta)]x = \\ &= 2kh(x, y)\sin(\theta + \frac{\Delta\theta}{2})\sin \frac{\Delta\theta}{2} + 2kx\cos(\theta + \frac{\Delta\theta}{2})\sin \frac{\Delta\theta}{2} \approx \\ &\approx kh(x, y)\Delta\theta\sin \theta + kx\Delta\theta\cos \theta, \end{aligned} \quad (8)$$

where the lastline results from an approximation for $\Delta\theta$ being much smaller than θ . This phase distribution is just equal to the phase of the projected fringes produced by the two coexisting beams. For small $\Delta\theta$ the height sensitivity of the phase difference is given by $\lambda/\Delta\theta\sin\theta$. The resultant distributions of the phase before and after the mirror rotation are subtracted from each other to produce the phase $\text{mod}(2\pi)$. After phase-unwrapping we obtain the phase distribution that is given by Eq. (8). Next the tilt component is subtracted to provide surface height distribution from the reference plane.

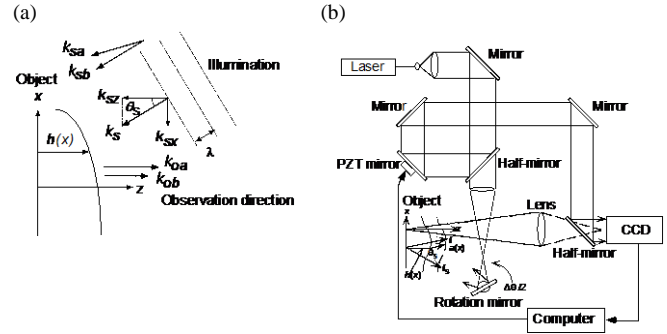


Fig. 3. (a) Principles and (b) setup of contouring.

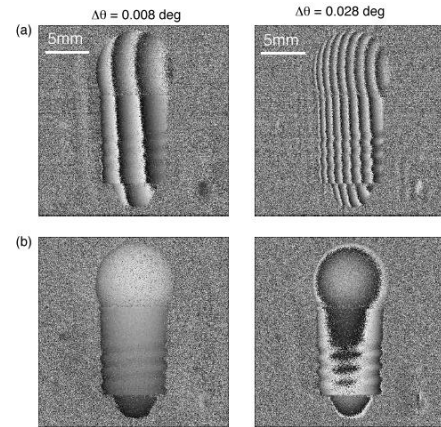


Fig. 4. Contours of a miniature bulb for different tilt angles.

Figure 4 represents the result obtained from the shape measurement of a miniature bulb painted white. The distributions of the phase difference shown in (a) contain the carrier component corresponding to the second term of the right-hand side of Eq. (8). By subtracting this component from the phase difference at 1024×1024 pixels before phase-unwrapping we align the reference plane parallel to the object plane as shown in Fig. 4(b). The resultant distribution contains noise associated with speckles. We suppressed this noise by extracting one point from each 2×2 matrix where the modulus of the product $|U_1 U_2^*|$ becomes maximum. This filtering is based on the fact that the phase value is more reliable for higher amplitude. The compressed data are then smoothed by averaging over each 2×2 matrix with final data pixels of 256×256 [5]. The 3D maps and the cross-sections through the bulb axis before (a) and after the filtering (b) are shown in Figures 5(a) and (b). This method of surface shape measurement could be easily applied to small objects by employing a microscope system mentioned above.

In the out-of-plane deformation measurement [6, 7] the illumination is fixed and the phase difference of the reconstructed waves before and after object deformation

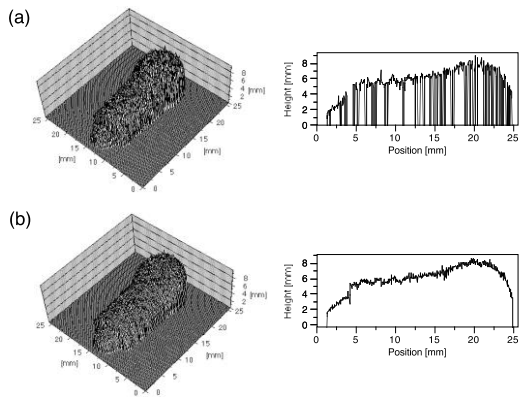


Fig. 5. Results from a miniature bulb under exponential filtering.

that depends on the vectors illustrated in Fig. 6. We denote the object displacement vector of the point (x, y) by $\mathbf{a}(x, y)$. If the speckle displacement is much smaller than their mean size, the phase difference becomes:

$$\Phi(x, y) = -(\mathbf{k}_s - \mathbf{k}_o) \cdot \mathbf{a}(x, y). \quad (9)$$

This condition means that the systematic phase change can be observed as a result of cancellation of a random phase variation between different speckles. It limits the measurement of in-plane displacement. To measure both surface shape and deformation of diffusely reflecting surfaces we built the optical system shown in Fig. 7. We employed a setup for image plane hologram so that limitation on the object size can be relaxed while ensuring high light flux incident on the CCD. The surface shape is measured by tilting the mirror for object illumination. This setup is the same as that of phase-shifting electronic speckle interferometry (ESPI), but the DH can also be used for 3D objects by virtue of numerical focusing. We need not refocus the imaging lens on the position of interest and have only to record the hologram once before and after object deformation and mirror tilt. We also have much more freedom of suppression of speckle noise because the phase difference is directly derived instead of correlation fringes detected in ESPI as mentioned above.

The results of experiments conducted for out-of-plane deformation of a square plate of aluminum with the size of $50 \times 50 \text{ mm}^2$ and 1 mm thick are shown in Fig. 8. The plate was pushed at its center while being supported at the circular edge. The phase difference (Fig. 8(a)) is the contour of out-of-plane displacement. The surface shape after total loading repeated 20 times is represented. The resolution is estimated to be $0.01 \text{ }\mu\text{m}$. For contouring a tilt of $\Delta\theta = 0.25$ degrees was added to $\theta_s = 45$ deg. After the removal of a carrier component the contours of (b) were obtained while (c) is the cross-section along the line indicated. The fluctuation of height is about 10 nm.

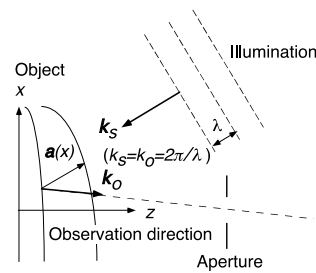


Fig. 6. Principles of deformation measurement.

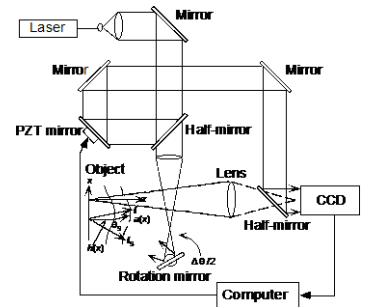


Fig. 7. Setup of deformation measurement.

which is an order of surface roughness of the specimen. Vibration analysis has also been conducted by time averaging the hologram intensity during the sinusoidal vibration over the exposure time much longer than the vibration period. At least three phase shifted holograms are recorded and reconstructed. The reconstructed image is modulated by the 0-order Bessel function, as in the classical holographic vibration analysis [8].

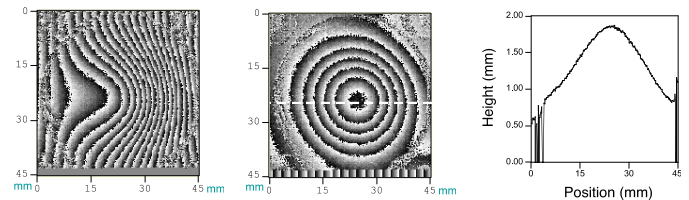


Fig. 8. (a) Phase deformation, (b) Removed tilt, (c) Cross-section along the line.

In this article we surveyed the principle and applications of phase-shifting digital holography that has improved performances of DH substantially. Since it delivers values of complex amplitude at the CCD plane directly without any filtering process, both derivation and processing of required information on the shape and deformation are straightforward and simple. A full number of CCD pixels is utilized for the final image with a quality much better than in the off-axis setup. We also proposed a new method of phase analysis with higher performance.

References

- [1] G. Bruning, D.R. Herriott, J.E. Gallagher, D.P. Rosenfeld, A.D. White, D.J. Brangaccio, *Appl. Opt.* **13**, 2693 (1974).
- [2] I. Yamaguchi, T. Zhang, *Opt. Lett.* **22**, 1268 (1997).
- [3] F. Zhang, I. Yamaguchi, L.P. Yaroslavsky, *Opt. Lett.* **29**, 1668 (2004).
- [4] I. Yamaguchi, *Optics and Lasers in Engineering* **39**, 411 (2003).
- [5] I. Yamaguchi, M. Yokota, *Opt. Eng.* **48**, 085602 (2009).
- [6] I. Yamaguchi, J. Kato, S. Ohta, *Opt. Rev.* **8**, 85 (2001).
- [7] I. Yamaguchi, J. Kato, H. Matsuzaki, *Opt. Eng.* **42**, 1267 (2003).
- [8] F. Zhang, J.D.R. Valera, I. Yamaguchi, M. Yokota, G. Mills, *Opt. Rev.* **11**, 5 (2004).

Recent advances in speckle decorrelation modeling and processing in digital holographic interferometry

Pascal Picart^{*1,2}

¹Laboratoire d'Acoustique de l'Université du Mans, CNRS 6613, Institut d'Acoustique - Graduate School (IA-GS), Le Mans Université, Avenue Olivier Messiaen, 72085 Le Mans Cedex 9, France

²École Nationale Supérieure d'Ingénieurs du Mans, rue Aristote, 72085 Le Mans Cedex 9, France

Received November 16, 2021; accepted December 23, 2021; published December 31, 2021

Abstract—Digital holography, and especially digital holographic interferometry, is a powerful approach for the characterization of modifications at the surface or in the volume of objects. Nevertheless, the reconstructed phase data from holographic interferometry is corrupted by the speckle noise. In this paper, we discuss on recent advances in speckle decorrelation noise removal. Two main topics are considered. The first one presents recent results in modelling the decorrelation noise in digital Fresnel holography. Especially the anisotropy of the decorrelation noise is established. The second topic presents a new approach for speckle de-noising using deep convolution neural networks.

Digital holography is a powerful approach for remote metrology at different scales (micro and macro) [1]. Holographic interferometry provides an optical path difference in the wrapped modulo 2π phase. The phase is connected to the scene/object/structure of interest and can be helpfully considered for many industrial purposes: roughness measurements [2], surface shape profiling [3], surface deformation [4] or vibration measurements [5]. Holographic interferometry has the benefit of being contact-less and provides full-field measurements. In addition, the use of light illumination makes it non-intrusive. High temporal resolution can be obtained when using high-speed cameras [5]. For example, holographic interferometry is adapted for the investigation of fundamental properties of transient mechanical waves propagating in complex metamaterials [6]. The use of long wavelength infrared radiations enables large deformation measurements, which are of interest for extended structures [7], by providing desensitization of holographic measurements by a factor of almost 20 [4].

From the practical point of view, the change in the optical phase from digitally reconstructed holograms is of interest and is obtained within modulo of 2π . Basically, the speckle pattern produced from the object surface under coherent illumination is modified as well as changes from its initial state. It follows that the phase from holograms is also speckled. Therefore, speckle decorrelation noise is included in phase changes and advanced filtering is required to get noise-free phase maps [8–9]. Recently, noteworthy progresses in the

understanding and modeling of the image-to-object relationship in holographic imaging has been obtained [1]–[12]. However, digital holographic interferometry is still limited by the requirement of fast data processing. For that, two main directions must be investigated: first, full modelling of speckle decorrelation noise and last, artificial intelligence (AI) [10] as a new paradigm to boost the computation time in digital holographic data processing.

Recently, we have addressed the first point and proposed modelling of speckle decorrelation in digital holographic interferometry [11]–[12]. For that, a complex coherence factor between two speckled images from two digitally reconstructed holograms is of interest and described by:

$$\mu = \frac{\langle A_1 A_2^* \rangle}{\sqrt{\langle |A_1|^2 \rangle \langle |A_2|^2 \rangle}}, \quad (1)$$

where A_1 and A_2 are the two considered digital holographic images from the reconstruction algorithm (discrete Fresnel transform or angular spectrum transfer function). The coherence factor is linked to the standard deviation of speckle noise according to [13] (for $|\mu| \geq 0.7$):

$$\sigma = \frac{7}{4}(1-|\mu|)^{2/5} \quad (2)$$

and that is why modeling $|\mu|$ is of main interest in expected development of future model-based de-noising algorithms. The computation of Eq. (1) must consider the point spread function of digital holography [14] which includes the sensor area (Np_x , with the N number of pixels and the p_x pixel pitch), the pixel surface width (Δx), the wavelength of light (λ) and the initial object-to-sensor distance (d_0). Then, experimental parameters under study can be related to the spatial frequencies produced by the object in the particular case concerned. As an example of our recent results, in the case of surface deformation measurement (mechanical loads, vibrations, thermal loads, pneumatic loads), we demonstrate that $|\mu|$ has the expression in Eq. (3):

* E-mail: pascal.picart@univ-lemans.fr

$$|\mu(u)| = \frac{\text{sinc}(\pi\Delta xu) \text{rect}\left(\frac{u-U_x/2}{U_x}\right) \otimes \text{sinc}(\pi\Delta xu) \text{rect}\left(\frac{u-U_x/2}{U_x}\right)}{\int_0^{U_x} \text{sinc}(\pi\Delta xu) du} \quad (3)$$

In Eq. (3), $U_x = Np_x/\lambda d_0$ is the cut-off spatial frequency of Fresnel holography, $\text{sinc}(x) = \sin(x)/x$ and $\text{rect}(x)$ is the rectangle function. The same relation holds for the y direction. The value of $|\mu|$ must be evaluated at the spatial frequency equivalent to the local slope of surface deformation [11]. Consequently, the speckle decorrelation noise is anisotropic and depends on both the dimensions of the sensor area and the local orientation of the fringes generated by the local surface slope of the deformation between the two holograms (refer to Fig. 1). This new result provides new opportunities for advanced de-noising methods in digital holographic metrology. Indeed, prior knowledge related to surface deformation could be used for predicting local noise and for processing adaptation. This would be very useful for high-speed holographic imaging because, in such a process, the number of pixels of the sensor is reduced and the decorrelation noise is stronger than in classical experiments.

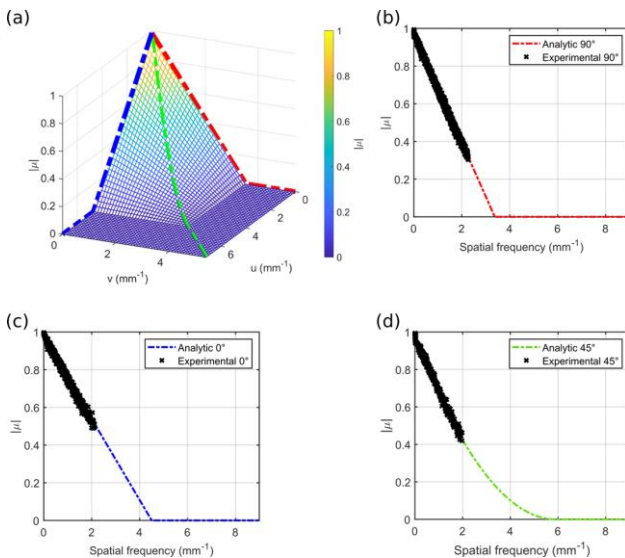


Fig. 1. Comparison between theory and experiments, (a) theoretical values of $|\mu|$, with the dashed blue line for the vertical fringes and the dashed red line for the horizontal orientation and the dashed green line for the inclined one, (b) comparison between experimental estimations of $|\mu|$ and theoretical values in the case of the horizontal fringes, (c) comparison between experimental estimations of $|\mu|$ and theoretical values in the case of the vertical fringes (d) comparison between experimental estimations of $|\mu|$ and theoretical values in the case of the 45° fringes; from [11].

For the past 10 years, artificial intelligence (AI) and deep learning based on convolutional neural network have emerged as very efficient tools in signal and image processing with applications in speech and language understanding, or image recognition. It has now impacted digital holography for computer-generated holograms [10]. Soon, deep learning will probably strongly influence

digital holography and its related post processing approaches. Especially, there is great interest in AI methods because they may strongly decrease the processing time for de-noising phase maps. Recently, we have demonstrated that the two-dimensional windowed Fourier transform (WFT2F) is the state-of-the-art of speckle noise removal in speckle metrology [15] (refer to Fig. 2). The main drawback is a relatively long processing time to deal with phase maps including 1024×1024 data points.

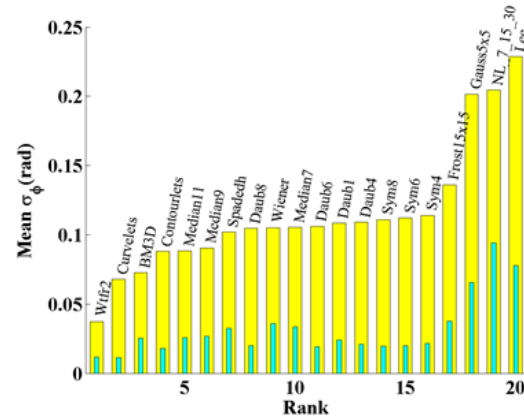


Fig. 2. Ranking of de-noising algorithms from the point of view of the standard deviation of the phase error; from [15].

To overcome such a limitation, we developed an approach based on deep learning [16]–[17]. One solution to improve de-noising with deep learning is to go deeper and to add more layers to the network. Despite higher capacity, overfitting and vanishing or exploding gradients arise as two main problems. The latter can be controlled by batch normalization and the use of skip connections such as in residual networks. But, to avoid overfitting even with regularization techniques, the amount of data is critical. Data augmentation generally helps in artificially increasing the amount of training data. Considering that a close relation does exist between the network depth and the size of convolutional filters (and the receptive field, consequently), the question of the depth requirement has not been thoroughly investigated.

The generalization power of machine learning algorithms is the “ability to perform well on previously unobserved inputs”. To do so, data are usually split into training, development, and test sets, with the latter consisting of unobserved noisy phase data.

In our first approach [16], we trained a DnCNN (deep convolutional neural networks) for speckle de-noising in holographic phase data. The network reaches good performances with the benchmark data in comparison to other de-noising techniques such as BM3D, DTDWT or WFT2F. That was demonstrated for most of the evaluated phase data [16]. In our last developments, the aim is to reduce the training time while reaching similar performance. To do so, databases for development and

validation were specifically designed and developed [17]. The main result is that a pre-trained model is not required unless the diversity and amount of simulated data are not consistent. In this case, the lack of data may be compensated by the pre-training. The experiments also demonstrated that very deep networks are not mandatory to use, and that four convolution blocks produce good performances when compared with WFT2F. Note that the advantage of reduced networks is the fact that they are fast to train. This study also addressed the issue of networks generalization. The paper [17] shows that the WFT2F algorithm continues to be the best one for phase images including strong noise (refer to Fig. 3). However, the baseline of WFT2F can be outperformed with our best model when considering experimental data. The deep learning approach was applied to experimental data from vibroacoustics based on on-line digital holography with a high-speed camera (refer to Fig. 4) and yielded excellent results compared to those provided by a scanning vibrometer [18].

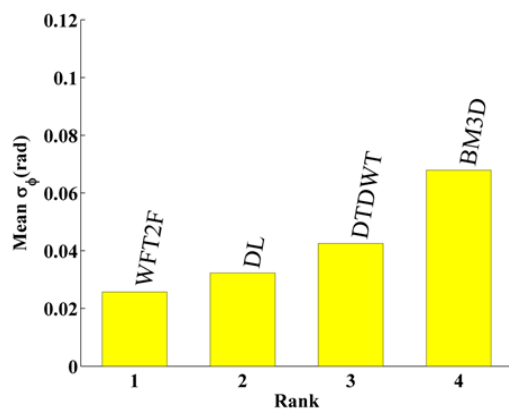


Fig. 3. Ranking of de-noising algorithms from the point of view of the standard deviation of the phase error; DL: our approach with deep learning; from [16].

In the future, we aim at investigating a multiplicative model. Improvement of speckle de-noising could be reached by combining the advantages of the two approaches and mixing in a noise estimator. To increase the amount of training data, we aim at implementing other data augmentation functions. Finally and additionally, a new database with an increased diversity of fringe images would be a matter of importance in learning the networks with a large diversity of phase fringe patterns.

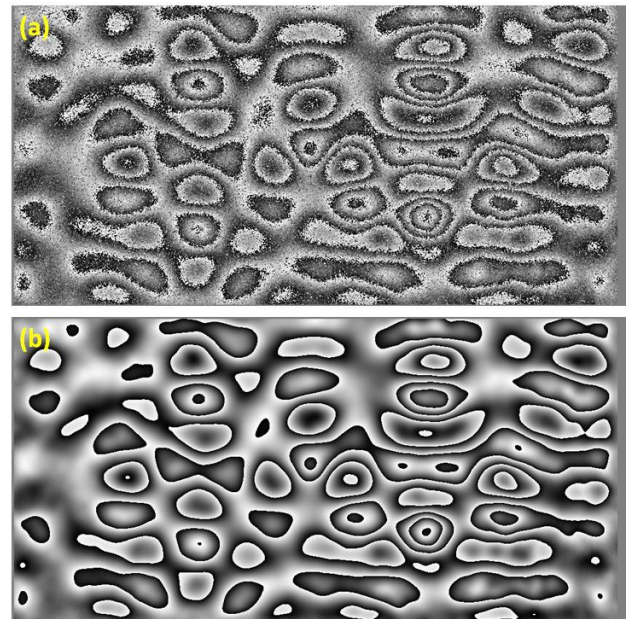


Fig. 4. (a) noisy phase map from the experiments in vibroacoustics, (b) de-noised phase processed from our deep learning approach; from [17].

References

- [1] P. Picart (ed.), *New techniques in digital holography* (John Wiley & Sons, 2015).
- [2] T.M. Biewer, J.C. Sawyer, C.D. Smith, C.E. Thomas, *Rev. Sci. Instr.* **89**, 10J123 (2018).
- [3] M. Fratz, T. Beckmann, J. Anders, A. Bertz, M. Bayer, T. Gießler, C. Nemeth, D. Carl, *Appl. Opt.* **58**(34), G120 (2019).
- [4] M.P. Georges, J.-F. Vandenrijt, C. Thizy, Y. Stockman, P. Queeckers, F. Dubois, D. Doyle, *Appl. Opt.* **52**(1), A102 (2013).
- [5] E. Meteyer, F. Foucart, M. Secail-Geraud, P. Picart, C. Pezerat, *Mech. Syst. Signal Process.* **164** (2022).
- [6] L. Lagny, M. Secail-Geraud, J. Le Meur, S. Montresor, K. Heggarty, C. Pezerat, P. Picart, *J. Sound Vib.* **461** 114925 (2019).
- [7] L. Valzania, Y. Zhao, L. Rong, D. Wang, M. Georges, E. Hack, P. Zolliker, *Appl. Opt.* **58**, G256 (2019).
- [8] V. Bianco, P. Memmolo, M. Leo, S. Montresor, C. Distante, M. Paturzo, P. Picart, B. Javidi, P. Ferraro, *Light: Sci. Appl.* **7**(1), 1 (2018).
- [9] V. Bianco, P. Memmolo, M. Paturzo, A. Finizio, B. Javidi, P. Ferraro, *Light: Sci. Appl.* **5**(9), e16142 (2016).
- [10] R. Horisaki, R. Takagi, J. Tanida, *Appl. Opt.* **57**(14), 3859 (2018).
- [11] E. Meteyer, F. Foucart, C. Pezerat, P. Picart, *Opt. Expr.* **29**(22), 36180 (2021).
- [12] M. Piniard, B. Sorrente, G. Hug, P. Picart, *Opt. Expr.* **29**(10), 14720 (2021).
- [13] P. Picart, S. Montresor, O. Sakharuk, L. Muravsky, *Opt. Lett.* **42**(2), 275 (2017).
- [14] P. Picart, J. Leval, *J. Opt. Soc. Am. A* **25**, 1744 (2008).
- [15] S. Montresor, P. Picart, *Opt. Expr.* **24**(13), 14322 (2016).
- [16] S. Montresor, M. Tahon, A. Laurent, P. Picart, *APL Photonics* **5**(3), 030802 (2020).
- [17] M. Tahon, S. Montresor, P. Picart, *Photonics* **8**(7), 255 (2021).
- [18] E. Meteyer, S. Montresor, F. Foucart, J. Le Meur, K. Heggarty, C. Pezerat, P. Picart, *Sci. Rep.* **11**(1), 1 (2021).

LCOS Spatial Light Modulator for Digital Holography

Wei jie Wu, Mike Pivnenko, Daping Chu*

Center for Photonics Devices and Sensors, University of Cambridge, Cambridge CB3 0FA, UK

Received November 14, 2021; accepted December 06, 2021; published December 31, 2021

Abstract—Liquid crystal on silicon (LCOS) spatial light modulator (SLM) is the most widely used optical engine for digital holography. This paper aims to provide an overview of the applications of phase-only LCOS in two-dimensional (2D) holography. It begins with a brief introduction to the holography theory along with its development trajectory, followed by the fundamental operating principle of phase-only LCOS SLMs. Hardware performance of LCOS SLMs (in terms of frame rate, phase linearity and flicker) and related experimental results are presented. Finally, potential improvements and applications are discussed for futuristic holographic displays.

The concept and method of holography were proposed by Polish scientist Mieczysław Wolfke in 1920 when he studied the possibilities of optical imaging of molecular structures [1], which were later independently discovered and developed by Dennis Gabor [2]. However, the real holographic display failed to implement due to the lack of strong and coherent light sources until lasers emerged in the 1960s [3]. Holographic display, named as a full parallax display technology in Benton's framework [4], can provide all four physical depth cues that the human brain can perceive (i.e. binocular parallax, motion parallax, accommodation, and convergence) [5]. It is eulogized as the 'holy grail' for three-dimensional (3D) displays due to its capability to deliver true 3D images for naked eyes.

The original holography utilizes the interference principle to record both amplitude and phase information of a 3D object on photographic films [6]. However, it was shown phase-field of holography functions could also be used to represent the spatial and optical properties of an object, with all depth cues, thus provide a vivid 3D sensation [8].

In 1967, Lohmann and Paris calculated a hologram by the computing power of a digital computer [9]. Following Goodman and Lawrence's idea of digital holography and Yaroslavskii and Merzlyakov's fundamental theory, the technique of computer-generated hologram (CGH) arose [10]. A CGH is a digital form of a suitable hologram pattern, calculated (typically based on Fourier transform) to represent the amplitude and phase information of the desired object, which supersedes the optical information recording process mentioned above. The CGH, which loads on an optical engine like a SLM in the form of 2D pixel arrays, is independent of the holographic recording material. Furthermore, the CGH calculation process can reproduce all different functions of diffractive optical

elements (ODE) and even manifest the information of non-existent objects, making it enormously useful for data manipulation, transmission, and replication. Due to this numerical-based feature, both amplitude and phase information can be separately extracted as amplitude-only and phase-only, respectively. As human eyes are incentive to phases, it is possible to use phase-only information in the form of phase-only CGH to reconstruct not only the positioning information but also the intensity of an object. Such phase-only CGHs can be uploaded as the information source on phase-only SLMs which are universally used in holographic displays during the object's image retrieve process. Various algorithms for CGH calculations have been developed over the years, from the primitive direct binary search (DBS), simulated annealing (SA) [11], Gerchberg-Saxton (G-S) [12], to other complex ones.

The first liquid crystal pixel array driving by silicon backplane was reported by the team of Ernstoff *et al.* in the early 1970s [13]. Shortly afterward, the first LCOS demo was shown by Crossland *et al.* in 1982 based on the field-effect of nematic liquid crystal [14]. Over the last forty years, LCOS devices have been intensively studied as a technology for SLMs in multifarious applications, such as holographic display, optical correlators [15], optical tweezers [16], and wavelength selective switches [17]. LCOS SLM acts as the optical engine in digital holography for both hosting the CGH and modulating the reference beam for image reconstruction. A phase-only LCOS SLM consists of two alignment layers, one liquid crystal (LC) layer for phase-modulating, and one electrode layer for signal-addressing [18,19]. The electrode layer is a pixel array, where the voltage of each pixel can be individually controlled according to the input signal, i.e. CGH. Due to the coordination of the electrode pixel voltage and local LC molecule rotation, the phase delay provides the optical information required at that pixel. For a reflective LCOS SLM, the pixelated electrode layer is made of aluminium mirrors; while for a transmissive LCOS SLM, the pixelated electrode layer is made of transparent conductors. Complementary metal-oxide-semiconductor (CMOS) silicon backplanes are used for reflective LCOS SLMs, which according to their memory accessing properties are either DRAM-based or more often SRAM-based [20].

The nematic LC is prevalently adopted in phase-only

* E-mail: dpc31@cam.ac.uk

applications due to its large birefringence and multilevel phase modulation ability [18, 19, 21-24]. When designing a suitable LC layer for LCOS for display applications, it is preferred to use the LC cell with the minimum thickness, larger splay elastic constant, and the smallest dielectric constant ratio on the premise of a 2π modulation depth and a proper LC response speed [25].

A disadvantage of using nematic LCs in phase-only LCOS SLMs is from its anti-parallel zero-twisted configuration. When the applied voltage is removed, apart from the slowdown of the LC molecules rotating back to their original state due to the viscous dragging force, the relaxation of the LC molecules within the mid-layer will be forced to the opposite direction because of the unwanted asymmetric backflows of the LC molecules within the two adjacent LC layers, which will further delay the optical response of the whole device [18]. As a result, the intrinsic LC relaxation time, which is the off-time when the applied voltage is removed, is several times longer than the on-time when a voltage is applied, resulting in a long frame time for the breakups in colour sequential operations [26] and image blurring during refreshing [28] as shown in Figure 1. A thinner LC layer thickness would moderate this issue [18]. However, to maintain a 2π modulation depth in a thin LC layer requires LC materials of high birefringence. An attempt for high birefringence mixture showed material instability at high temperatures and photochemical degradation under blue light exposure [27]. Alternatively, high frame rates can be achieved by using nematic LCs with moderately high birefringence and low visco-elastic ratio in combination with a voltage adjustment method and LCOS SLMs with a refresh rate higher than 2,000 frames per second (fps) were reported [28].

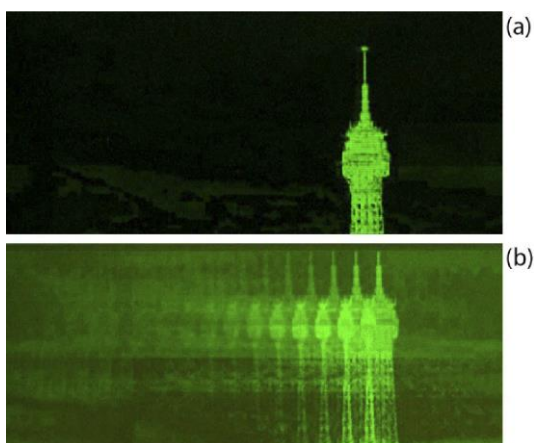


Fig. 1. Blurring effect of a refreshing image on (a) a fast LCOS with a response time of $\sim 700 \mu\text{s}$ and (b) a slow LCOS device with a response time of $\sim 30 \text{ ms}$ [28].

Nematic LCs are known to be electro-optically nonlinear,

and AC driving schemes, especially digital pulse width modulation (PWM) driving schemes, can make the LC molecule directions and hence the phase delays wobbling in a given phase level, which is known as phase flicker [29]. Such an instability is due to the competition between the corresponding LC molecules' relaxation and the change in their electrical driving force, leading to temporal rotational fluctuations of the forced LC molecules and modulated phase instability. Figure 2 shows an example of phase flicker induced by a digital PWM driving waveform.

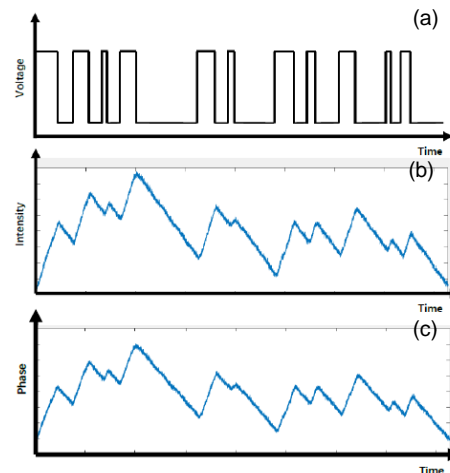


Fig. 2. (a) The PWM driving waveform, (b) the corresponding instant intensity, and (c) the instant phase calculated at grey level 120 within a single modulation period.

Although in a continuous display, the effect of phase flicker is less obvious as the flicker frequency is normally higher than that can be perceived by human eyes [30]. However, in instant holographic reconstruction or other non-display applications, phase flicker is the culprit of instantaneous errors, especially crosstalk. Furthermore, phase flicker can also lead to phase overlapping between adjacent phase levels, limiting the number of the phase levels and hence the information bandwidth that an LCOS SLM can deliver.

To minimise the phase flicker, the signal pulse of each grey level should be arranged as uniformly as possible. Averaged phase flicker of 0.0018π was reported in a $6 \mu\text{m}$ pixel LCOS SLM for 8-bit infrared modulation with manually optimized driving patterns [31]. In which, the phase flicker was reduced to such a level to eliminate overlap of the adjacent phase levels for 8-bit modulation, as shown in figure 3. As a result, a 17.7% improvement on the holographic reconstructed image in terms of RMS contrast ratio was achieved by a 50% flicker reduction together with phase linearisation, as shown in Fig. 4. This is followed by a deep learning method of pattern optimization for an averaged phase flicker of 0.0011π and 10-bit modulation [32]. Other LCOS driving methods including high-frequency field inversion and DC balancing failed to reach the same optimization effect [33]. Finally, the phase flicker can be reduced through changing LC

properties. A study successfully reduced the flicker up to 80% by increasing the LC's viscosity when cooling it to $-8\text{ }^{\circ}\text{C}$, but the switching speed become much slower [34].

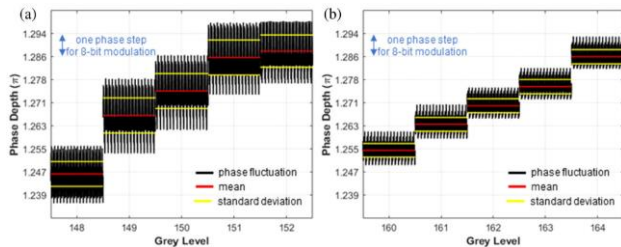


Fig. 3. Phase fluctuations at phase depth around 1.26π (a) before and (b) after optimization on phase linearity and phase flicker [31].

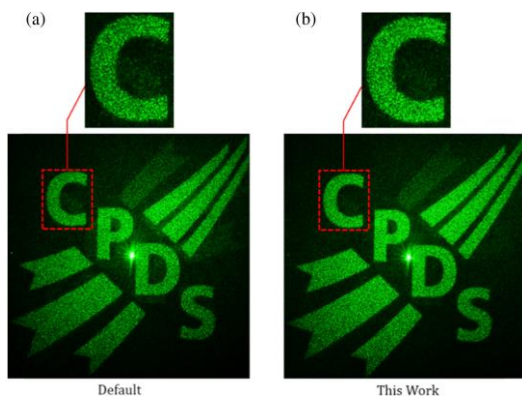


Fig. 4. Holographic reconstructed image (a) before and (b) after optimization from work [31].

In conclusions, the market of digital holography using phase-only LCOS SLMs will continue to grow. After the introduction of 'Metaverse', LCOS SLMs are bound to play a vital role for a more parallel, synchronized, and immersive end-user experience. At the same time, the requirements for LCOS SLMs will be more stringent. As high display quality, in terms of high refresh rate, high display resolution and low phase flicker, is the essential for the promised holographic world. Better driving techniques for a faster switching, smaller phase flicker and higher phase levels should be attempted. Finally, phase retrieving algorithms for CGH calculations should be further developed to incorporate phase flicker and other effects if possible.

References

- [1] M. Wolfke, *Physikalische Zeitschrift* **21**, 495 (1920).
- [2] D. Gabor, *Nature* **161**, 777 (1948).
- [3] H. Haken, *Light and Matter* **5**, 14 (1970).
- [4] S. Benton, *Selected Papers on Three-dimensional displays*, SPIE Press (2001).
- [5] X. Liang *et al.*, 3D holographic display with optically addressed spatial light modulator, 3DTV-CON 2009 – 3rd 3DTV Conference (2009).
- [6] J. Chen, W. Cranton, M. Fihn, *Handbook of Visual Display Technology* (Springer 2012).
- [7] D. Rogers, *The chemistry of photography: From classical to digital technologies* (Royal Society of Chemistry, 2007).
- [8] S. Reichelt *et al.*, *Proc. SPIE* **7690**, 76900B (2010).
- [9] A.W. Lohmann, D. Paris, *Appl. Opt.* **6**, 1739 (1967).
- [10] J.W. Goodman, R.W. Lawrence, *Appl. Phys. Lett* **17**, 77 (1967).
- [11] D.C. O'Brien, R.J. Mears, W.A. Crossland, *Appl. Opt.* **33**, 2795 (1994).
- [12] R.W. Gerchberg, W.O. Saxton, *Optik* **35**, 237 (1972).
- [13] M. Ernstoff, A. Leupp, M. Little, and H. Peterson, Liquid crystal pictorial display, Proceedings of the 1973 International Electron Devices Meeting, IEEE, 548 (1973).
- [14] W.A. Crossland, P.J. Ayliffe, P.W. Ross, *Proc SID* **23**, 15 (1982).
- [15] M. Tang, J. Wu, Optical Correlation recognition based on LCOS, International Symposium on Photoelectronic Detection and Imaging 2013, Optical Storage and Display Tech., 8913 (2013).
- [16] A. Hermerschmidt *et al.*, Holographic optical tweezers with real-time hologram calculation using a phase-only modulating LCOS-based SLM at 1064 nm, Complex Light and Optical Forces II, International Society for Optics and Photonics, 30282 (2008).
- [17] M. Wang, *et al.* *Photonics* **4**, 22 (2017).
- [18] Z. Zhang, Z. You, and D. Chu, *Light Sci. & Appls.* **3**, e213 (2014).
- [19] D. Yang, and S. Wu, *Fundamentals of liquid crystal devices, 2nd edition* (Wiley 2015).
- [20] B. Prince, *Semiconductor memories: A handbook of design, manufacture, and application, 2nd edition* (John Wiley & Sons 1996).
- [21] J.C. Jones, *Liquid crystal displays, Handbook of optoelectronics: Enabling Technologies, 2nd ed.* (CRC Press 2018).
- [22] A. Adrian *et al.*, *Phys. Wave Phenom.* **27**, 67 (2019).
- [23] S.M. Kelly, M. O'Neil, *Liquid crystal for electro-optic applications, Handbook of advanced electronics and photonic materials and devices* (2000).
- [24] Y. Ji *et al.*, *J. SID* **22**, 4652 (2015).
- [25] X. Chang, *Solution-processed ZnO nanoparticles for optically addressed spatial light modulator and other applications, Ph.D. thesis* (University of Cambridge, Cambridge 2019).
- [26] E. Moon *et al.*, *Opt. Express* **22**, 6526 (2014).
- [27] G. Aad *et al.*, *Phys Rev. D* **83**, 4389 (2011).
- [28] M. Pivnenko, K. Li, D. Chu, *Opt. Express* **29**, 24614 (2021).
- [29] H. Yang, D.P. Chu, *Opt. Express* **27**, 24556 (2019).
- [30] P. Bach-Y-Rita *et al.* *Int. J. Hum. -Comput. Interact* **15**, 285 (2003).
- [31] Y. Tong, M. Pivnenko, D. Chu, *Appl. Opt.* **58**, G248 (2019).
- [32] Y. Tong, M. Pivnenko, D. Chu, *Adv. Dev. & Instr.* **1**, 10 (2020).
- [33] H. Yang, D. Chu, *Opt. Express* **27**, 24556 (2019).
- [34] J. García-Márquez, *et al.* *Opt. Express* **16**, 8431 (2008).

Distortion correction for wide angle holographic projector

Jędrzej Szpygiel, Maksymilian Chlipała, Rafał Kukołowicz, Moncy Idicula, Tomasz Kozacki*

Faculty of Mechatronics, Warsaw University of Technology, 8 Św. A. Boboli St. 75, 02-525 Warsaw, Poland

Received October 15, 2021; accepted December 16, 2021; published December 31, 2021

Abstract—This letter presents a distortion correction method enabling a distortion minimized, large size image in a wide angle holographic projector. The technique applies numerical predistortion of an input image used for hologram generation. It is based on estimation of distortion coefficients by comparing optically a reconstructed point test chart with the original one. Obtained experimental results prove that the technique allows reconstruction of high-quality image.

A lensless holographic projector built with a phase SLM (Spatial Light Modulator) enables the reconstruction of a high quality, aberration free image [1]. The main limitation of the display is a small projection angle, which is closely related to the pixel pitch of the used SLM. For an SLM with a pixel pitch size of 3.74 μm the projection angle is $\pm 4.8^\circ$. Thus, it should be increased to display larger images.

In state-of-the art limited projection, the angle is addressed by two solutions, utilizing a spherical illumination module [2] or a 4F imaging system [3, 4]. In the first technique the projection angle depends on the radius of curvature of the illuminating beam. The method is limited by the overlap of reconstructed images of higher diffraction orders. In the second approach, two lenses with different focal lengths demagnify the pixel pitch of the SLM. The limitation of the 4F method is the focal length ratio, as the demagnification increases the projector becomes bulkier.

Recently we have proposed a wide-angle holographic projector with a single lens and efficient hologram generation utilizing complex coding, and nonparaxial diffraction [5]. The characteristic feature of optical systems using a lens is the formation of aberrations. The most problematic and visible for a wide-view-angle holographic projector is the aberration of distortion, which needs to be compensated.

There are two main approaches of aberration correction: (i) using additional physical optical elements or a wavefront sensor and a deformable mirror and (ii) utilizing numerical correction by means of algorithms and digital image processing. The disadvantage of the first approach is its high cost, time consuming alignment and non-adaptivity. Numerical methods are attractive since the hologram is in most cases computer generated or there is an access to the complex object wavefront. Zehao He *et*

al. proposed a technique that detects distortion basing on the position of points regionally divided and corrects it by means of planar and phase divergence correction factors [6]. In the solution, the image is divided into subregions, for which correction factors are calculated individually, and correction is made by pre-calibrating images before projection. Another approach was proposed by Kaczorowski *et al.*, in which the aberrations are corrected by means of a phase mask composed of 13 Zernike Polynomials [7]. The phase mask is uploaded onto the SLM, and its effectiveness is optimized by using two proposed algorithms - a hybrid genetic steepest descent and a heuristic variant of steepest descent. The mask maximizes the peak intensity of the point and minimizes the spread of pixels around the center, while imaging a point object. Zehao He *et al.* avoided the computational complexity of Zernike polynomials by implementing the angular spectrum algorithm and treating the image distortions as additional distribution superposed onto a computer-generated hologram [8]. In the work, the wavefront needed for eliminating the aberrations was acquired by a four-step phase shifting algorithm, which resulted in a reduced correction time.

Most solutions present in the literature require iterative algorithms of complex mathematic structure, which increase the correction time and computational requirements. The method proposed in this paper is based on a single pre-calibration step and pre-distorting the image in such a way that the distortion introduced by the system will be eliminated. The distortion coefficients are determined by detecting and comparing the position of projected test chart points to the desired ones. The radial and tangential distortions are considered. In this regards, the Fitzgibbons model is used, since it allows to describe much larger radial distortion with lower order terms. The assumed model of distortion can be presented by the following equations:

$$x_d = x_u + x_u k r^2 + q(r^2 + 2x^2) + 2p x y, \quad (1)$$

$$y_d = y_u + y_u k r^2 + 2q x y + p(r^2 + 2y^2), \quad (2)$$

where x_d , y_d and x_u , y_u are the distorted and undistorted coordinates respectively, k , p and q are the radial and tangential distortion coefficients. In order to measure image distortion, its coefficients are estimated by the

* E-mail: tomasz.kozacki@pw.edu.pl

displacement of a projected rectilinear grid of points. Next, the obtained data are used to pre-distort an image before projection to cancel the system's distortion. Since the distortion is the feature of the optical setup and does not depend on the projected image, only a single calibration step is needed. Firstly, the hologram of a test chart in a form of points array is displayed on the SLM. Then, by means of digital image processing the coordinates of points are detected. Since the ideal image is known, the desired spatial distribution of the points can be calculated for known projection parameters, such as projection distance, size of the SLM, camera pixel pitch, and wavelength. In order to calculate the distortion that influences the projected image, the ideal and detected points are compared and their corresponding coordinates are put into the following matrix equation:

$$\begin{bmatrix} k \\ p \\ q \end{bmatrix} = \begin{bmatrix} x_u r^2 & 2xy & (r^2 + 2x^2) \\ y_u r^2 & (r^2 + 2y^2) & 2xy \end{bmatrix}^+ \cdot \begin{bmatrix} x_d \\ x_d \end{bmatrix}, \quad (3)$$

where “+” denotes a pseudo-inverse matrix, since the matrix with unknown coefficients is not a square one, a pseudo-inverse matrix has to be calculated. What is more, since the detected distorted points do not follow the exact mathematical model of a distortion, an approximation is necessary to avoid a contradictory system of equations. These calculations provide the best fitting radial and tangential distortion coefficients. In order to compensate the distortion of the optical setup a pre-distortion of the image before projection is needed, so the distortions cancel each other out. The input image is processed and projected by a holographic display system.

The proposed pre-distortion approach is applied in an image generation framework of wide-angle holographic projection display, which is presented in Fig. 1, to improve image quality. It employs laser source ($\lambda = 632,8 \text{ nm}$), plane wave illumination, 4K phase only LCoS SLM (HOLOEYE Photonics AG, model GAEA-2, reflective phase only Liquid Crystal on Silicon microdisplay, resolution 4160×2464 , $3.74 \mu\text{m}$ pixel size) for hologram displaying, Fourier Transforming lens L_p (focal length $F_p = 35 \text{ mm}$) for enlarging viewing angle, and rectangular spatial frequency filter to enable complex wave encoding. The lens ensures a wide projection angle α_x , which depends on the size of a used SLM and optical power of the lens as $\alpha_x = \sin^{-1}(B_s/F_p)$. For $F_p = 35 \text{ mm}$ and projection distance $z_p = 700 \text{ mm}$ image has the size $306 \text{ mm} \times 161 \text{ mm}$. The filter has two tasks: to decode the complex phase-coded information [9] and to pass only 1st diffraction order of the SLM. In our system the SLM is tilted and information order is separated from the zero order by adding a spatial carrier frequency to the hologram.

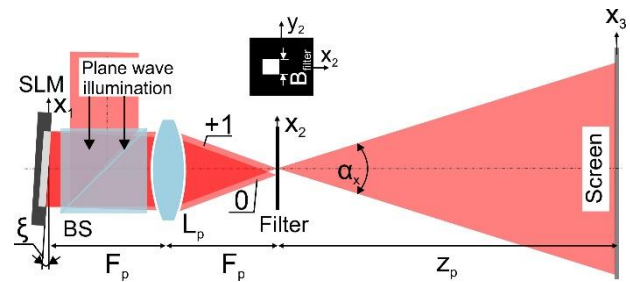


Fig. 1. Scheme of a wide-angle holographic projection display.

The diagram for the hologram generation algorithm is presented in Fig. 2. It consists of five steps: (i) pre-distortion of the image with calculated coefficients using Equation 3, (ii) nonparaxial propagation of an optical wavefield from the image plane (x_3, y_3) to the filter plane with Angular Spectrum Compact Space Bandwidth Product method [10], (iii) band-limiting the signal in the frequency domain to one fourth of the system bandwidth, (iv) calculation of Fast Fourier Transform giving optical field in SLM plane (x_1, y_1), and (v) generation of Double Phase Hologram [9]. The steps (iii) and (iv) are included for clear understanding of the algorithm only. The step (iv) does not have to be performed. In the algorithmic part of step (iii) there is an access to the Fourier Transform of the field at the filter plane.

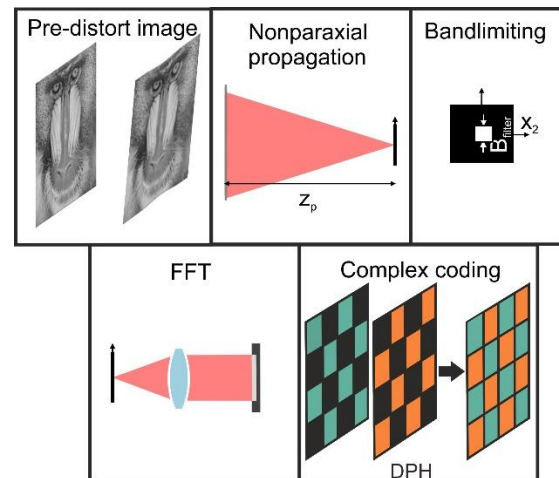


Fig. 2. Hologram generation algorithm.

To find the distortion coefficient of holographic display, the image of a test points chart consisting of 13 columns and 9 rows was generated and projected through the system at 7 mm and captured by a 4K CCD camera. The detected coordinates were compared to the ideal ones and the distortion coefficients were calculated using Equation 3, giving the following values:

$$k = 5.514 \cdot 10^{-9}, \\ p = -3.112 \cdot 10^{-6}, \quad q = -6.598 \cdot 10^{-6}.$$

The test chart was then pre-distorted with the same distortion coefficients values but with the opposite signs. In Fig. 3 the distorted and corrected images of the test chart are superimposed and colored to visualize the distortion correction. Blue dots correspond to the distorted image and red ones to the corrected one.

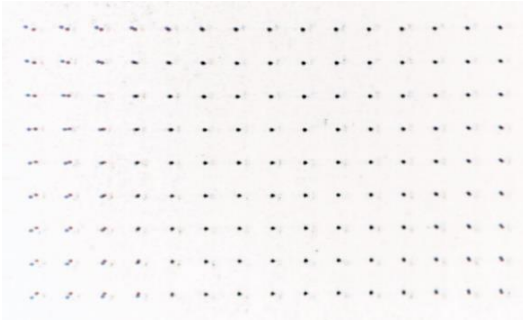


Fig. 3. Test chart before (blue) and after distortion correction (red).

The coordinates of the corrected chart were detected and compared to the ideal and distorted images. The quality of correction was also measured by comparing the mean displacement error of the distorted coordinates from the ideal to the corrected ones. The RMS error of displacement diminished significantly from 27 to 13 pixels, showing the range of correction.

The proposed method was investigated optically by reconstructing a 2D “Mandrill” image. For this, two holograms were generated and reconstructed at distance $z_p = 700$ mm. The first hologram was calculated from the original image and the second from the pre-distorted image. Fig. 4 presents photos captured by the zoom lens camera. The obtained results show that the method allows for obtaining a high quality distortion corrected image.

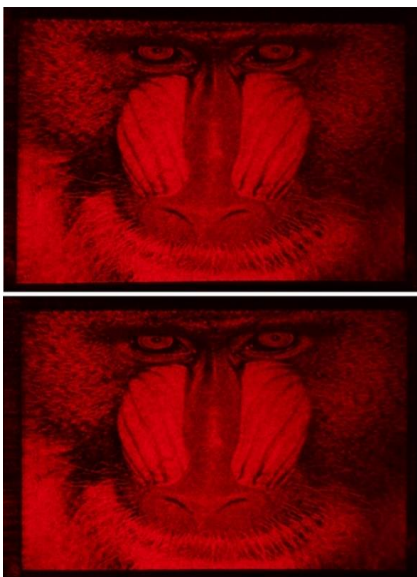


Fig. 4. Optically reconstructed “Mandrill” image before (upper) and after distortion correction (lower).

In conclusion, this letter presents a distortion compensation method allowing us to reconstruct a distortion minimized, large-size image in a wide-angle holographic projector. The technique is based on single pre-calibration of the setup and pre-distorting the image. The pre-calibration is realized in two steps. First, optical reconstruction of the point array test chart is obtained in the display and acquired by a CCD. Next, the positions of points in space are numerically detected, compared with the reference ones and distortion coefficients k , p , r are calculated. The calculated distortion coefficients are applied to pre-distort the image so the distortion introduced by the system will be cancelled out. Optical reconstructions prove that the proposed method allows for obtaining a high quality distortion corrected image.

Fundings: Politechnika Warszawska; Narodowe Centrum Nauki (UMO-2018/31/B/ST7/02980).

References

- [1] M. Makowski, Experimental Aspects of Holographic Projection with a Liquid-Crystal-on-Silicon Spatial Light Modulator, in *Holographic Materials and Optical Systems*, M. Kumar, ed. (IntechOpen, 2019).
- [2] H. Pang, A. Cao, W. Liu, L. Shi, Q. Deng, *Appl. Opt.* **58**, 8713 (2019).
- [3] Y. Qi, C. Chang, J. Xia, *Opt. Express* **24**, 30368 (2016).
- [4] E. Buckley, *J. Display Technol.* **99**, 1 (2010).
- [5] M. Chlipała, T. Kozacki, H. Yeom, J. Martinez-Carranza, R. Kukołowicz, J. Kim, J. Yang, J. Choi, J. Pi, C. Hwang, *Opt. Lett.* **46**, 4956 (2021).
- [6] Z. He, X. Sui, L. Cao, G. Jin, "Image-Distortion Correction Algorithm for Computer-Generated Holographic Display," 2018 IEEE 27th International Symposium on Industrial Electronics (ISIE), 1331 (2018).
- [7] A. Kaczorowski, G.S. Gordon, A. Palani, S. Czerniawski, T.D. Wilkinson, *J. Display Technol.* **11**(7), 596 (2015).
- [8] Z. He, X. Sui, G. Jin, L. Cao, *IEEE Trans. Industr. Inform.* **15**, 6162 (2019).
- [9] O. Mendoza-Yero, G. Mínguez-Vega, J. Lancis, *Opt. Lett.* **39**, 1740 (2014).
- [10] T. Kozacki, K. Falaggis, *Appl. Opt.* **55**, 5014 (2016).

Improved playback uniformity of random-phase free holograms by pixel separation method

Michał Makowski,^{*1} Tomoyoshi Shimobaba²

¹Faculty of Physics, Warsaw University of Technology, 75 Koszykowa, 00-662 Warsaw, Poland

²Graduate School of Engineering, Chiba University, 1-33 Yayoi-cho, Inage-ku, Chiba 263-8522, Japan

Received October 11, 2021; accepted December 17, 2021; published December 31, 2021

Abstract—Random-phase free computer-generated holograms offer excellent quality of virtually noise-free playback of low-frequency images, but have limited efficiency in the case of highly contrast binary images with dominant high spatial frequencies. The introduction of weak random phase allows partial suppression of this problem, but causes strong noise in the outcome. Here we present the influence of a pixel separation technique on the uniformity of far field reconstructions from such random-phase free holograms. We show improved image quality with no additional speckle noise.

Most commonly used Computer-Generated Holograms (CGH) are computed with a degree of randomized phase. This allows the utilization of a full spectrum of possible angles of diffraction after the hologram in order to fulfill intensity constraints in the output plane [1, 2]. On the other hand, such an approach comprises inevitable random interferences of light rays forming adjacent points of the holographic image [3]. This problem can be partly solved by introducing a periodical void between image points by a pixel separation method [4].

Random-Phase Free (RPF) holograms have the unique property of correct image reconstruction at Fresnel distances without the introduction of randomized phase and consecutive noise [5]. Their disadvantage is poor rendering of high-contrast, binary images where high spatial frequencies are dominant. Although iterative error diffusion algorithms of their optimization were presented [6], their usage comprises a significant increase of the computational burden. A method of improving the uniformity of replayed intensity patterns from the RPF CGHs would be advantageous.

Here we present the application of a non-iterative technique of pixel separation used for the RPF CGHs. It assumes splitting a given input image into a set of subframes, each of which contains a subset of pixels. Usually the choice of pixels is random or periodical, but in every case all subframes combined (summed) give the exact copy of the input frame. The aim of eliminating a set of pixels in subframes is to create void spaces between image points reconstructed from the hologram. Such voids introduce zero amplitude spots in the image space and as

* E-mail: michal.makowski@pw.edu.pl

such eliminate some of the uncontrolled interferences, thus contributing to the suppression of speckle noise, which was described in details [3]. Exemplary input image (*USAF-1951 resolution test*) used in this work and its four subframes are shown in Fig. 1.

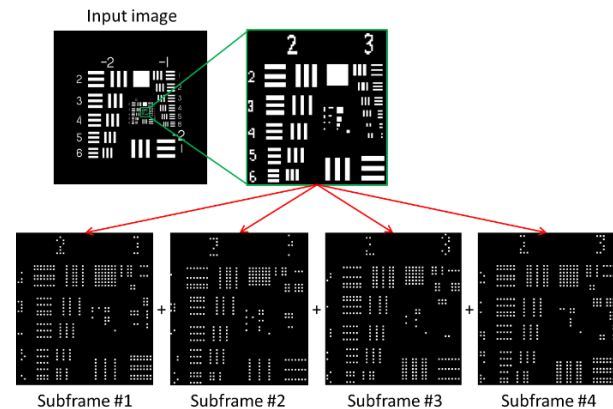


Fig. 1. Test input image for holographic computation and its subframes with pixel separation value $N=2$.

The distance between adjacent illuminated (i.e. non-void) pixels is called the separation constant N , here $N=2$. The total number of the subframes is equal to N^2 , here 4.

In this section we will present the results of numerical simulations of holographic image reconstructions from CGHs computed with four methods. Method 1 assumes the computation of a RPF hologram from a non-pixel-separated input frame [5]. In this case no error diffusion or random phase inclusion was made. Methods 2 and 3 are modifications of Method 1 in which the input field is altered by adding a weak random phase in the range of $\pm\pi/4$ and $\pm\pi/2$, respectively. Method 4 is our proposed method, which uses pixel separation with $N=2$. The numerical reconstructions of the encoded *USAF-1951* test image are gathered in Fig. 2.

All images were computed with an angular spectrum propagation method [7, 8] on matrices of 2048^2 complex samples on in-house software. The sampling was set at $8\ \mu\text{m}$ and the wavelength was fixed at $633\ \text{nm}$. The propagation distance was $200\ \text{mm}$, which did not violate the Nyquist limit and thus ensured that the maximal angles of diffraction enabled the light from all corners of the CGH to converge in the played back on-axis image.

seems to be a good compromise between the requirements to fill the insides of the objects and to keep the noise at a low level.

	SSIM	noise contrast
Method 1	18%	53%
Method 2	64%	43%
Method 3	70%	44%
Method 4	54%	29%

Fig. 3. Statistics of image quality for the compared methods.

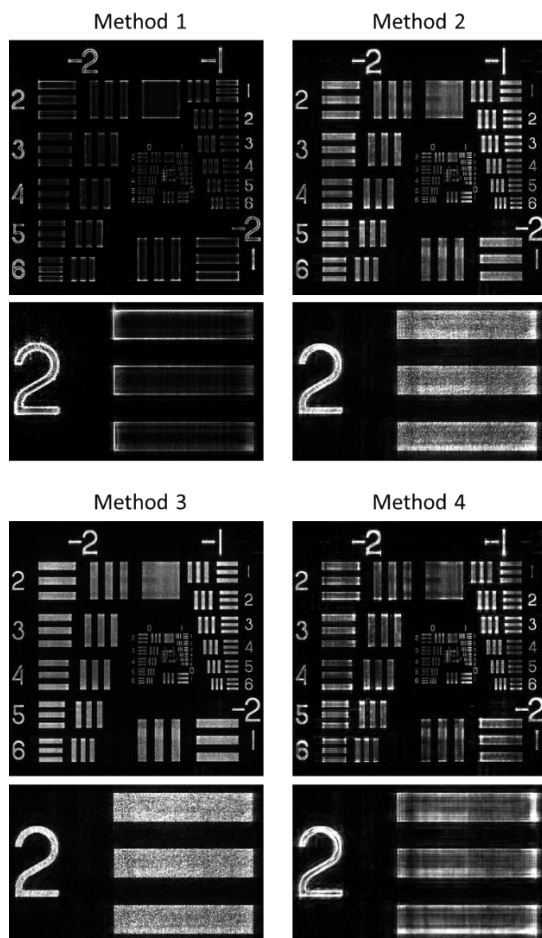


Fig. 2. Numerical holographic reconstruction of the test image with four compared methods. Close-ups of the 2nd group are shown for noise estimation.

From the qualitative analysis of Fig. 2 one can notice that Method 1 performs very poorly and requires serious upgrade. The previously presented methods of improving image uniformity based on the addition of random phase (Method 2 and 3) inevitably introduce grain-like noise, which stands in conflict with the main advantage of the RPF holograms, i.e. virtually no speckle noise. On the other hand, they significantly improve the uniformity of the insides of the bars seen in the *USAF* pattern. Method 4

The quantitative analysis of the numerical results is given in Fig. 3. The proposed methods features the lowest noise level of all compared, while the structural similarity (SSIM) is on the middle level, which makes this stand in full agreement with subjective qualitative analysis.

The proposed method of pixel separation applied to RPF holograms has proven to be effective at little additional computational cost, mostly devoted to the calculation of three additional CGHs. The disadvantage of this method is experimental complexity which lies in the necessity of quickly displaying four sub-holograms on a spatial light modulator in order to get them integrated in the detector, e.g. human eye. Exemplary CGHs of subframes of the used *USAF-1951* test image are shown in Fig. 4, while their numerical reconstructions showing fragmented sub-images are shown in Fig. 5.

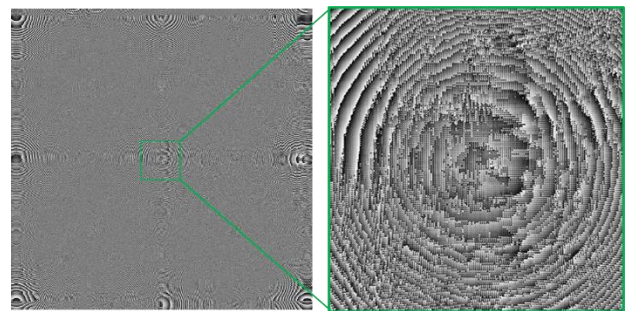


Fig. 4. Exemplary CGH of a pixel-separated subframe with its magnified central region.

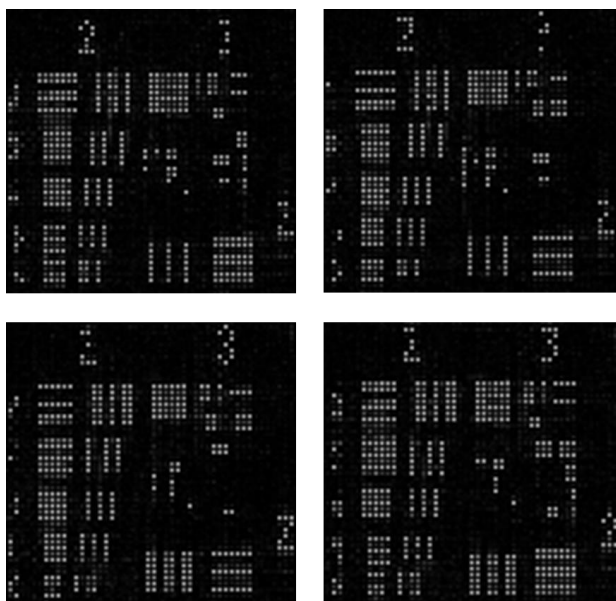


Fig. 5. Central magnifications of the intensity fields reconstructed from the four sub-holograms of the test image.

The experimental validation, as well as finding the optimal value of pixel separation distance and/or optimal pattern of inter-pixel voids will be the matter of our future research.

References

- [1] J.W. Goodman, *Introduction to Fourier optics* (Roberts and Company, 2005).
- [2] R.W. Gerchberg, W.O. Saxton, *Optik* **35**, 237 (1972).
- [3] M. Makowski, *Opt. Express* **21**, 29205 (2013).
- [4] I. Ducin, T. Shimobaba, M. Makowski, K. Kakarenko, A. Kowalczyk, Jaroslaw Suszek, M. Bieda, A. Kolodziejczyk, M. Sypek, *Opt. Comm.* **340**, 131 (2015).
- [5] T. Shimobaba, T. Ito, *Opt. Express* **23**, 9549 (2015).
- [6] T. Shimobaba, T. Kakue, Y. Endo, R. Hirayama, D. Hiyama, S. Hasegawa, Y. Nagahama, M. Sano, M. Oikawa, T. Sugie, T. Ito, *Opt. Express* **23**, 17269 (2015).
- [7] M. Sypek, *Opt. Comm.* **116**, 43 (1995).
- [8] K. Matsushima, T. Shimobaba, *Opt. Express* **17**, 19662 (2009).

Numerical optimization of writing computer-generated holograms in threshold media

Mateusz Sadowski, Michał Makowski*

Faculty of Physics, Warsaw University of Technology, 75 Koszykowa, 00-662 Warsaw, Poland

Received August 03, 2021; accepted November 13, 2021; published December 31, 2021

Abstract—Recent developments in binary photo-magnetic materials showed efficient and ultra-fast rewriting of holograms where the intensity threshold allows for a dense, sub-diffraction limit packing of hologram points. This paper describes the numerical optimization of the process of writing and reconstructing of 2-D images in a binary-phase computer-generated holograms stored in the said threshold-like medium. Global free parameters optimization of the writing process is shown, including the intensity threshold level, propagation distance, hologram spot size and the shape of the boundary regions of the written spots. We present the optimal set of parameters for the best possible writing quality.

Computer-generated holography (CGH) allows real-time design, writing and playback of phase-only or amplitude-only holograms. Usually it is realized by computer-aided design, connected with the frame-by-frame display on a spatial light modulator (SLM), most likely based on the liquid-crystal-on-silicon (LCoS) technology. Although this scheme is well known and widely used, some intrinsic limitations of LC-based displays, like slow refresh rates and lack of internal memory, slow down the progress in CGH development for final applications in holographic television of the future. For those reasons, novel and faster materials for dynamic CGH are being developed. Among them are photo-magnetic materials capable of light-induced patterning at 10 GHz rates with femtosecond laser pulses [1, 2]. The area of switched magnetic domains in this process is related with the intensity and focusing of the fs pulse, since the medium has a certain intensity threshold [3]. For this reason, the CGH design and writing parameters must be optimized for such binary, threshold-like materials. In this work we present the outcome of such initial optimization, leading to the best possible writing and playback scheme in future experiments.

In this paper, the simulation of diffraction and propagation was done using the Angular Spectrum Method [4]. The test binary-phase iterated [5] hologram presenting a test “8” symbol with a rectangle was oversampled by 16 times and rewritten with a threshold. As seen in Fig. 1, the produced pattern was numerically illuminated with a convergent beam focusing at the pre-set propagation distance. This numerical experiment

clearly resembles a typical configuration of the holographic projection of 2-D images [6, 7].

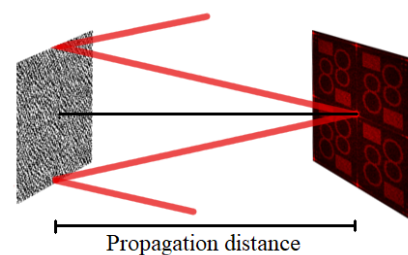


Fig. 1. Simulating the propagation of a holographic pattern illuminated with a convergent beam.

Each sample (pixel) of the input holographic pattern was rewritten into a square cell of 16 by 16 pixels, as seen in Fig. 3. This oversampling has allowed us to simulate the threshold writing by binarization of a Gaussian beam pattern within the cell, as depicted by the green line in Fig. 2. In a separate test additional gradient samples, called superpixels were added on the transition between 1 and 0 values representing gradual change of intensity. This parameter potentially allows one to investigate the fine differences in the performance of materials with different profiles of boundaries between written and not-written domains, which often depends on the layer thickness [1].

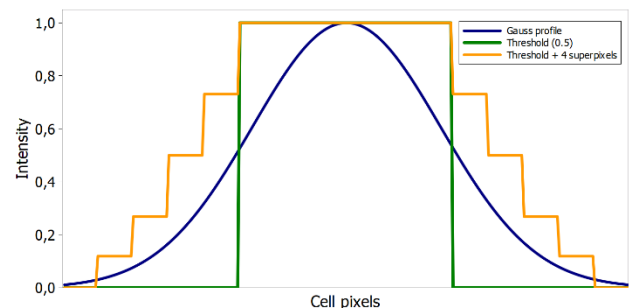


Fig. 2. Comparison of intensity in oversampled representations of the elementary cell of the hologram.

* E-mail: michal.makowski@pw.edu.pl

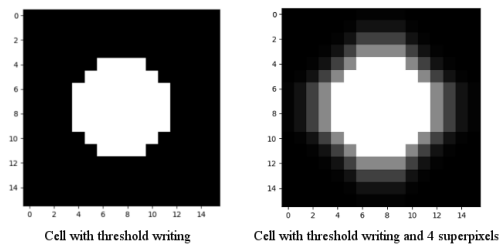


Fig. 3. Examples of hologram cells with gradient superpixels.

Although the simulation has many variables which can be changed the analysis and optimization of parameters has been done only for values most impactful on the quality of the reconstructed image. The tested parameters were: • Propagation distance, • Value of threshold in cell writing, • Width of the writing gaussian beam, • Size of the pattern, • Number of superpixels.

The base parameters were used for each of the simulations:

- Wavelength: 632.8 nm,
- Pattern size: 30×30 mm,
- Propagation / screen distance: 1 m,
- Oversampling: 16×16,
- Superpixels: 0,
- Threshold value: 0.5,
- Gaussian beam width: 0.08 mm.

In Fig. 4 exemplary far field reconstructions of the test hologram for different sets of the simulation parameters are presented. Plot A represents the default parameters of the simulation. Plot B shows the changes due to compressing the pattern into a 15x15 mm square, expanding the output image. Plot C is visibly dimmer and slightly larger thanks to 2.5x larger propagation distance. Plot D displays the change in intensity distribution caused by 4 additional superpixels in cells of the pattern.

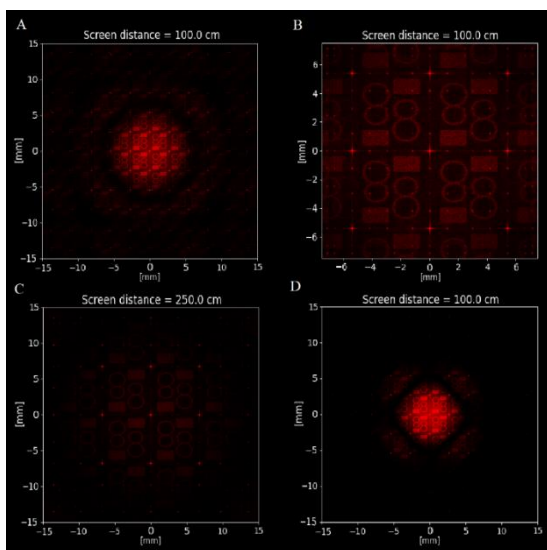


Fig. 4. Examples of far field intensity reconstructions for different sets of simulation variables.

Parameters of the reconstructed images in each simulation series were statistically analysed from each obtained numerical far field playback. Diffraction efficiency in 1st order, contrast and speckle noise were calculated after separating the image from the background using filtering and then combined into a joint statistic quality (Q) value representing the weighted performance of the playback. The Q value is defined as follows:

$$Q = \frac{100 * D.Eff. + 0.5 * Cont. + 2.5 * \frac{1}{Speckle\ Noise}}{4}$$

Figures 5–9 contain graphs showing the results of tested relations. Right side graphs present the Q statistics while on the left there are presented separated data points representing the normalized diffraction efficiency, contrast, and speckle noise (brown, green and blue circles, respectively) for each series. Value of 1 means the best achieved result in the graphs on the left.

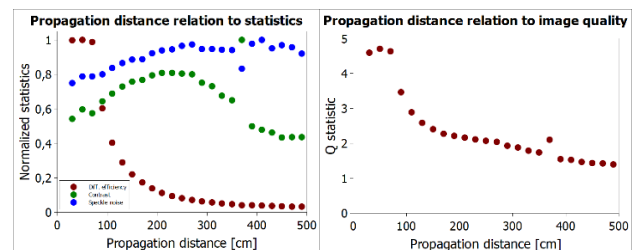


Fig. 5. Influence of the propagation distance on the image statistics.

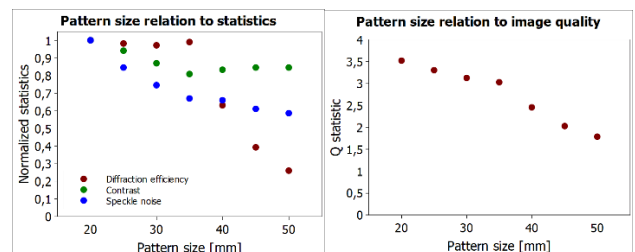


Fig. 6. Influence of the hologram size on the image statistics.

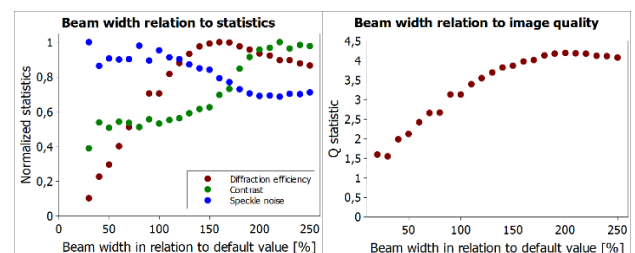


Fig. 7. Influence of the writing beam width on the image statistics.

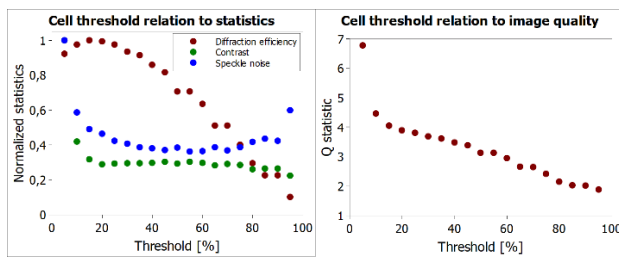


Fig. 8. Influence of the threshold value on the image statistics.

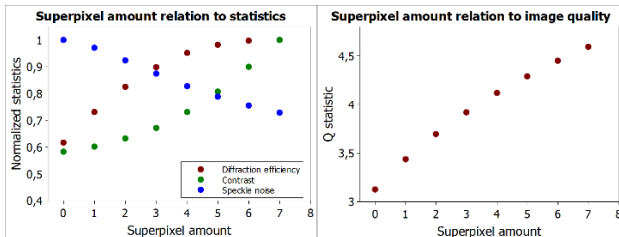


Fig. 9. Influence of the superpixel count on the image statistics.

Due to threshold and beam width parameters being linked the conclusion from our results is that the cells of the pattern should be filled as much as possible while remaining circular. Superpixels can be used to fill the remaining gaps. Smaller patterns have better diffraction efficiency and speckle noise. Closer propagation allows for better diffraction efficiency but makes the image less clear because of the 0th order of diffraction.

Using the changes, we have achieved a statistically optimized result shown in Fig. 10. Plot A represents the default parameters. Plot B uses the optimized parameters allowing it to achieve a higher diffraction efficiency and less noise while sacrificing some contrast due to the 0th order. Plot C shows simulation using the same parameters at further distance achieving higher contrast at the cost of the other statistics. The elementary hologram cell formed from the optimal set of parameters is shown in Fig. 11.

We have shown that the optimization of the holographic recording in a threshold-like medium requires a careful selection of parameters of the writing beam. No global optimum was found to satisfy all quality measures. Based on the preselection of the most critical quality measure in a given experiment, the optimal set of beam properties can be taken based on the graphs presented here. The fine adjustment of the parameters of the process allows for obtaining a better and clearer image with superior diffractive efficiency, which is significant for future holographic experiments on exotic materials exhibiting the intensity threshold.

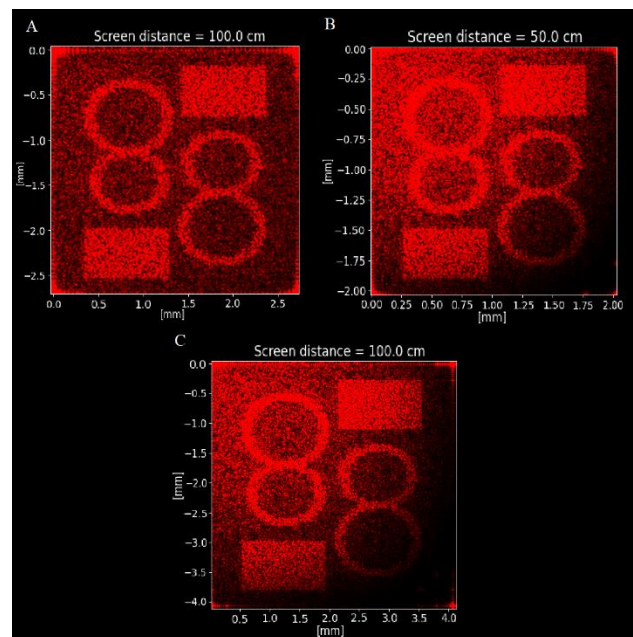


Fig. 10. Far field reconstructions with default and optimized parameters.

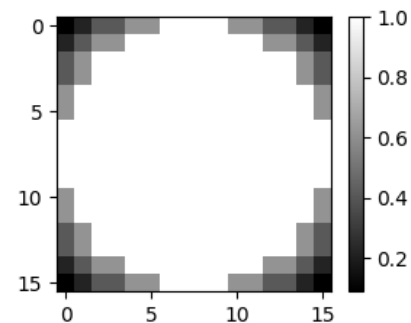


Fig. 11. The optimal configuration of the elementary writing cell of the hologram.

References

- [1] A. Stupakiewicz, K. Szerenos, D. Afanasiev *et al.*, *Nature* **542**, 71 (2017).
- [2] J. Starobrat, A. Frej, J. Bolek, R. Trybus, A. Stupakiewicz, M. Makowski, *Opt. Lett.* **45**, 5177 (2020).
- [3] V. Ostroverkhov *et al.*, *Jap. J. App. Phys.* **48**.3S1, 03A035 (2009).
- [4] K. Matsushima, T. Shimobaba, *Opt. Express* **17**, 19662 (2009).
- [5] F. Wyrowski, O. Bryngdahl, *JOSA A* **5.7**, 1058 (1988).
- [6] I. Ducin, T. Shimobaba, M. Makowski, K. Kakarenko, A. Kowalczyk, Jarosław Suszek, M. Bieda, A. Kolodziejczyk, M. Sypek, *Opt. Comm.* **340**, 131 (2015).
- [7] M. Makowski, *Opt. Express* **21**, 29205 (2013).

Neural-network based approach to optimize THz computer generated holograms

Mateusz Surma,^{*1} Mateusz Kaluza,¹ Patrycja Czerwińska,¹ Paweł Komorowski,² and Agnieszka Siemion¹

¹*Faculty of Physics, Warsaw University of Technology, Koszykowa 75, 00-662 Warsaw, Poland*

²*Institute of Optoelectronics, Military University of Technology, Kaliskiego 2, 00-908 Warsaw, Poland*

Received October 14, 2021; accepted December 20, 2021; published December 31, 2021

Abstract—Terahertz (THz) optics often encounters the problem of small f -number values (elements have relatively small diameters comparing to focal lengths). The need to redirect the THz beam out of the optical axis or form particular intensity distributions resulted in the application of iterative holographic methods to design THz diffractive elements. Elements working on-axis do not encounter significant improvement while using iterative holographic methods; however, for more complicated distributions the difference becomes meaningful. Here, we propose a totally different approach to design THz holograms, utilizing a neural network based algorithm, suitable also for complicated distributions.

Fast developing terahertz (THz) technology finds applications in many fields of science and industry such as optics, medicine, security, or non-destructive testing [1–3]. Each new application requires specific optical elements that will allow for full use of the potential of THz radiation under given conditions. Thus, new solutions allowing to meet market needs are still requested. Nowadays, thin diffractive optical elements (DOEs) are used instead of thick refractive lenses. The continuous phase changes, kinoform coding method, allow to redirect the whole electromagnetic radiation into a single diffraction order, which significantly increases the efficiency of the THz diffractive structures [4–5].

More advanced DOEs can be designed as synthetic holograms. Synthetic holography is based on calculating complex transmittance that, when illuminated, redirects the radiation to form the image of an object. Therefore, designed wavefront shapes can be more advanced and complex compared to classic holography [5] or designing DOEs using analytical equations.

Regrading applicational requirements, synthetic holography mostly utilizes different kinds of iterative methods like the Gerchberg-Saxton, also called the Iterative Fourier transform Algorithm (IFTA), or the ping-pong algorithms [6–7]. Such algorithms perform a number of iterations propagating the wavefront between the hologram and the image planes. In each plane a particular amplitude distribution is forced, while the phase is being optimized. Thus, the generated phase distribution in the hologram plane results in forming the

desired, previously defined, amplitude distribution in the image plane.

Nowadays, the additive manufacturing technique is more and more often used to create the designed THz DOEs. Such techniques use polymer materials in the form of powder, wire (filament), or resin to deposit material layer by layer. In the case of lower THz frequencies additive techniques guarantee a sufficiently high resolution of the manufacturing process [8]. Such techniques allow both for fast prototyping and good optical properties of fabricated components due to the high performance of polymer materials in the THz radiation range [9].

This work compares the THz phase kinoform lens with a synthetic hologram structure designed with iterative techniques. Moreover, we present a synthetic hologram generated by a neural network (NN). The network has been trained by the backpropagation method with stochastic gradient descent using an adaptive learning rate (ADAM). It is an innovative solution in the field of designing synthetic holograms. A detailed description of the algorithms, as well as the source code can be found in the Wolfram Community blog post [10]. The first approach to optimize DOEs with this method was described only using numerical simulations in [11]. The performance of the NN structure was simulated numerically. Then, a three-dimensional model of the hologram was created and fabricated using the additive manufacturing technique.

Three different structures were designed using different approaches to obtain DOEs with the design wavelength $\lambda = 2.141$ mm (frequency 140 GHz), the diameter $D = 100$ mm and focal length $f = 700$ mm. The first method calculated the phase distribution (φ) according to the analytical non-paraxial converging lens formula:

$$\varphi(x, y) = -\frac{\lambda}{2\pi} \sqrt{x^2 + y^2 + f^2}, \quad (1)$$

where λ is the design wavelength, f is the focal length, x and y are the cartesian coordinates.

The second approach was to design a structure using the iterative method based on the ping-pong algorithm. The single iteration process consisted of forward propagation from the hologram plane to the image plane, where the desired amplitude distribution – the focal spot

* E-mail: mateusz.surma.dokt@pw.edu.pl

diameter – was forced. Then, backward propagation from the image plane to the hologram plane was performed. The process was repeated 10 times and the desired intensity patterns in both planes were applied. All propagations were realized using the modified convolution method [12]. The iterated hologram was also calculated for different forced amplitudes with smaller diameters of the desired focal spots to investigate the influence of the focal spot size on the phase distribution patterns.

In the third approach, a structure realizing the same diffractive task – on-axis radiation focusing – was designed by means of neural network training.

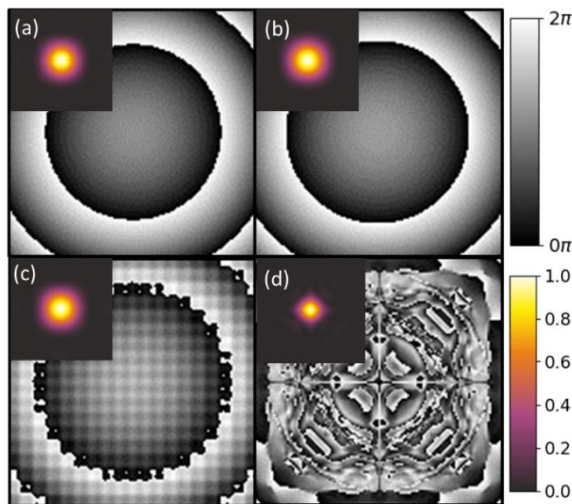


Fig. 1. The comparison of the converging lens created by: a) an analytical phase kinoform equation (Airy disc size – 36.6 mm) and iterative synthetic holograms with different predefined focal spot diameter sizes b) $d = 18$ mm, c) $d = 9$ mm and d) synthetic hologram calculated by NN (predefined 18 mm). Theoretical intensity distributions are presented in the left top corners of images; they have been normalized according to the scale presented in the right bottom, while the phase distributions are described by the greyscale palette presented in the top right.

In all simulations a grayscale 128×128 px bitmap has been generated. Each pixel contained a value from 0 to 255 that corresponded to a phase retardation from 0 to 2π .

The phase distributions, corresponding to the theoretical equation (a) with an Airy disc size equal to 36.6 mm, the iterative algorithm with a forced focal spot diameter of 18 mm (b) and 9 mm (c) as well as neural network based design with the forced focal spot equal to 18 mm (d) are presented in Fig. 1. Additionally, the simulated theoretical intensities in the focal planes ($f = 700$ mm) are shown in the insets. As it can be seen in the top row, the difference between the phase maps generated by the theoretical equation and iterative algorithm is unperceivable for the human eye. The difference in Fig. 1c is, however, much more likely to be noticed. The obtained phase map is more grainy and noisy, which is caused by reducing the size of the target focal spot used in the iteration process significantly below the diffraction

limit. On the other hand, the obtained focal spot remained unchanged (its diameter cannot be reduced below the beforementioned diffraction limit), even though the forced focal spot was smaller than the Airy disc size. Since the phase distribution complexity and granularity have direct influence on the quality of manufacturing, the size of the forced focal spots should be carefully considered. The neural network based designed hologram phase distribution has a completely dissimilar and individual look that does not remind any of the previous ones in Fig. 1. Theoretically, the intensity of the focal spot simulated by NN approach creates a hologram that forms an image having a smaller diameter than the analytically designed one and introduces only a small background interference pattern around it.

The height of each pixel, corresponding to the bitmap's phase distribution φ , can be calculated according to the following equation (2):

$$h(x, y) = \frac{\varphi(x, y) \lambda}{2\pi(n-1)}, \quad (2)$$

where n is the refractive index of the material and φ is the phase distribution expressed in the cartesian coordinates.

The height map must be transformed into a real structure by creating a proper 3D file and a manufacturing method. To assure proper manufacturing quality a sampling of $900 \mu\text{m}$ was chosen. Therefore, the 3D model of the synthetic hologram was created with a total horizontal size of $115.2 \times 115.2 \text{ mm} + 5 \text{ mm}$ frame and a maximal height of $4.17 \text{ mm} + 0.5 \text{ mm}$ substrate. Two different designing techniques of 3D models were analyzed. The first approach (simplest) is based on extruding each point (node) represented by pixel into the designed height level. Next, the nodes are connected forming triangles in the 3D space (for .stl file format). Thus, the obtained model representing the bitmap interpolates values between nodes. This solution can be applied to oversampled models; however, for small matrices such an approach introduces large errors. This method was used to manufacture a converging lens defined by the theoretical equation, where the phase distribution is smooth enough to assure proper quality of the DOE. The second method was based on building 3D blocks representing each pixel (each composed of 12 combined triangles) and extracting blocks to a calculated height level. This second method is crucial in extending relatively small matrix size bitmaps, guaranteeing a significantly better representation of the bitmap in the case of NN synthetic holograms according to the carried out simulations. Images obtained for NN 3D models with both methods are shown respectively in Fig. 2a and 2b.

The NN synthetic hologram was fabricated using the additive manufacturing technique – FDM (Fused Deposition Modelling) with the filament Cyclic Olefin Copolymer (COC), characterized by high stiffness, low deformation and extremely good optical properties. Its

absorption coefficient is very low in the whole THz spectral range (for 140 GHz it is equal to 0.05 cm^{-1}), and its refractive index was equal to 1.513. These properties guarantee extraordinary possibilities in the fabrication of phase THz DOEs. The horizontal and vertical resolutions of the 3D printer were equal to $450 \mu\text{m}$ and $100 \mu\text{m}$, respectively. It allowed to precisely represent each pixel of the bitmap in the manufacturing process. An analytically designed kinoform lens was produced in the same way.

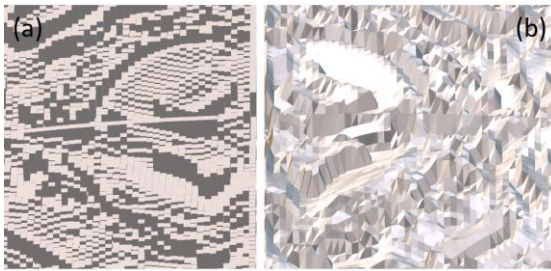


Fig. 2. The 3D models of the NN synthetic hologram rendered by two different methods: a) extending each bitmap's pixel separately, b) interpolation of nodes with respect to pixels' height levels. Significant differences between models can be noticed.

Both the NN and the analytically designed kinoform lens were verified in the experimental setup. It consisted of a frequency multiplier (WR-5.1 from Virginia Diodes) emitting radiation at 140 GHz, parabolic mirror forming a quasi-plane wave, as well as a tested lens and a detector (Schottky diode with a hemispherical silicon lens). The precise position of the focal plane was experimentally adjusted for the minimal diameter and maximal intensity of the focal spots and slightly differed from the designed focal length, due to the imperfections of the incident wavefront. Raster scans of the intensity distributions were registered in XY plane (perpendicular to the optical axis) and are presented in Fig. 3.

Both structures allowed to obtain sharp focal spots in the desired positions. A classic off-axis diffractive lens generated from the analytical equation forms a nice round focal spot within the diffraction limit. The structure based on neural network design gives also a small and well focused spot. The background is larger than for classic DOE, but the intensity distributions were normalized, so taking into account the fact that the NN based structure had a smaller maximal intensity in the focal spot, it could result in larger background noise. Nevertheless, an extremely non-intuitive and non-predictable phase distribution can successfully focus the radiation into a focal spot slightly larger (by 0.6 mm according to their FWHMs, equal to 13.6 mm and 14.2 mm, which corresponds to the 32.2 mm and 33.7 mm Airy disc size, respectively) unlike in the case of a classic DOE lens.

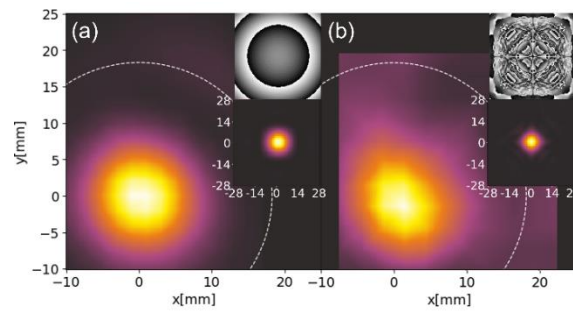


Fig. 3. The experimental results. The registered intensity (normalized) distributions for: (a) the lens designed according to the analytical equation, corresponding to Fig. 1a and (b) the NN-based algorithm, corresponding to Fig. 1d. The white circles denote the size of an Airy disk for the designed structures ($\lambda = 2.141 \text{ mm}$, $f = 700 \text{ mm}$, $D = 100 \text{ mm}$, circular aperture). In the insets – the structures phase maps and intensity distributions in the focal plane are shown for both cases.

Concluding, the converging lens designed by the NN algorithms was successfully developed and experimentally verified. The proposed converging lens has a totally different phase distribution, which is abstract and non-intuitive, especially comparing to the converging kinoform lenses and iterated holograms. The experimental results of both analytical equation based and NN based structures have shown that the proposed NN holographic lens is generating the focal spot as good as a classical lens. The larger focal spot size for the NN structure can result from scattering and shadow effect due to the fact that details of the phase map are much smaller than its height. However, this novel approach is opening new possibilities in the designing process of diffractive optical elements for THz radiation. From the manufacturing point of view it is crucial to adapt a 3D model to the complexity of phase transmittance to ensure a faithful representation of the phase map, which was realized by extending each pixel in the bitmap separately.

The research was funded by the National Science Centre, Poland under the OPUS-18 programme (2019/35/B/ST7/03909).

References

- [1] Y. Tao, A. Fitzgerald, V. Wallace, *Sensors* **20**(3), 712 (2020).
- [2] J. O'Hara, S. Ekin, W. Choi, I. Song, *Technologies* **7**(2), 43 (2019).
- [3] L. Yu *et al.*, *RSC Advances* **9**(17), 9354 (2019).
- [4] A. Siemion, *Sensors* **21**(1), 100 (2020).
- [5] A. Siemion, *J. Infrared Millim. Terahertz Waves*, **40**(5), 477 (2019).
- [6] M. Surma, I. Ducin, P. Zagrajek, A. Siemion, *Appl. Sci.* **9**(4), 659 (2019).
- [7] S. Banerji, B. Sensale-Rodriguez, *Scientific Reports* **9**(1), 5801 (2019).
- [8] J. Sun, F. Hu, *Int. J RF Microw Comput Aided Eng.* **30**(1) (2020).
- [9] E. Castro-Camus, M. Koch, A.I. Hernandez-Serrano, *J. Appl. Phys.* **127**(21), 210901 (2020).
- [10] https://community.wolfram.com/groups/-/m/t/2028026?p_%20479%20p_auth=blBLb5d
- [11] P. Komorowski *et al.*, *Opt. Expr.* **29**(7), 11243 (2021).
- [12] M. Sypek, *Opt. Comm.* **116**(1-3), 43 (1995).

From digital holographic microscopy to optical coherence tomography – separate past and a common goal

Arkadiusz Kuś,* Wojciech Krauze, and Małgorzata Kujawińska

*Warsaw University of Technology, Institute of Micromechanics and Photonics, Faculty of Mechatronics,
St. A. Boboli 8 st., 02-525 Warsaw, Poland*

Received December 19, 2021; accepted December 28, 2021; published December 31, 2021

Abstract—In this paper we briefly present the history and outlook on the development of two seemingly distant techniques which may be brought close together with a unified theoretical model described as common k-space theory. This theory also known as the Fourier diffraction theorem is much less common in optical coherence tomography than its traditional mathematical model, but it has been extensively studied in digital holography and, more importantly, optical diffraction tomography. As demonstrated with several examples, this link is one of the important factors for future development of both techniques.

Sixty years after Leith and Upatnieks published their paper describing off-axis holography [1], the technique is widely used in its digital version. The most common and interesting area of digital holography (DH) application is microscopy and biomedicine [2]. The integrated phase of the measured object provides valuable, label-free information which is directly related to e.g. dry mass in cells. In many cases the technique allows to replace fluorescence and due to its quantitative nature provides a plethora of new methods for cell characterization based on measurement and not just observation.

Optical coherence tomography (OCT), on the other hand, is a thirty years younger technique, which uses low-coherence interferometry to produce a qualitative two-dimensional image of refractive index gradient in tissue microstructures [3–4]. It is suitable to *in vivo* measurement configuration and its use in tomographic imaging of the retina was a milestone in ophthalmology [5].

When we look at the initial development of both techniques, it might seem that the link was distant at best, especially when we compare an analog holographic measurement process to point scanning time-domain OCT [4]. However, both techniques are in fact related through the same theory which links the K-space of the specimens scattering potential to object projections acquired in transmission or reflection configuration [6–7]. In this paper we show that holographic imaging in the microscopic scale and the OCT measurement are much closer to one another than it is often thought of and the techniques may be brought down to a common mathematical model to benefit from each other's

developments. We will start with a description of holographic microscopy.

As it has been described in works by Wolf [8–9], information about an analysed sample can be encoded in a complex amplitude of the plane wave that propagates through the specimen. After passing through the object, this wave can be decomposed into a sum of two waves: un-scattered wave U_0 , which is the same as the illuminating beam, and the U_s wave, scattered by the object. Both waves are summed in the hologram plane and are coded with the plane reference wave U_r .

According to the Huygens–Fresnel principle, once the plane wave from a single illumination direction interacts with a sample, each scatterer in the specimen generates a scattered spherical wave that propagates in every direction. In the case of digital holographic microscopy (DHM), only a portion of this wave is recorded with an optical system. The scattered wave (U_s) corresponds to a part of the Fourier spectrum of the scattering potential $F(R)$ of the measured object (Eq. 1).

$$F(R) = -k_0^2(n^2(R) - n_m^2) \quad (1)$$

The 2D information from the hologram may be mapped in the Fourier space onto the Ewald sphere (Fig. 1a) which represents a full scattered wave with the radius of curvature $k_0 = 2\pi/\lambda$. The information captured by the DHM from a single direction of illumination fills only a part of this sphere i.e. a single arc in 2D – (its extent is limited by the numerical aperture (NA) of the imaging system) and for this reason the retrieval of the refractive index with this method is highly inaccurate and DHM is generally considered a 2½D technique. Nevertheless, a simple measurement system (as illustrated in Fig. 2a) makes the technique highly accessible and practical [10]. However, should a series of different viewing perspectives of the object be acquired, the Fourier space becomes filled with data and depending on the projection acquisition scenario, the information is sufficient for a valid refractive index reconstruction. Such an approach is commonly known as optical diffraction tomography (ODT). Illuminating the stationary sample with a tilted beam allows to collect a larger part of the scattered wave without increasing the NA of the imaging objective [11]. To reconstruct the refractive index with this approach,

* E-mail: arkadiusz.kus@pw.edu.pl

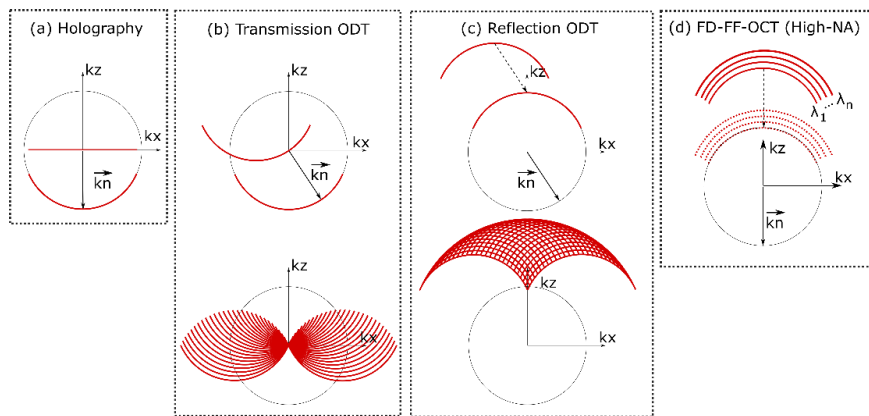


Fig. 1. Fourier space mapping based on different projection acquisition scenarios: a) simple holography, b) limited angle optical diffraction tomography, c) reflection ODT and d) Fourier domain full field optical coherence tomography realized with high numerical aperture (NA).

one must shift each part of the retrieved scattered wave to its origin described by the illumination vector \mathbf{kn} (Fig. 1b). The measurement system in this case is more complicated as an additional scanning element is required in the illumination part of the object beam such as a galvanometer mirror and an optical system to image the mirror in the sample plane, as indicated in Fig. 2b [11].

Apart from rotating the illumination, it is common practice to also (or only) rotate the sample [12], which provides more isotropic reconstruction resolution due to more uniform Fourier space coverage [13–14]. Nevertheless, a significant portion of information, which is back-scattered by the illuminated sample is lost due to imaging in transmission and what is more, this configuration is only suitable for *in vitro* or *ex vivo* measurements. For this reason it is often beneficial to perform ODT in reflection [15] as in Fig. 1c and use a much simpler configuration of the microscope [16]. However, retrieving only high frequencies as in Fig. 1c does not, in practice, allow access to information on refractive index changes, which is mostly located in the low-frequency region. One of the directions currently pursued is to maximize the coverage of the data in the Fourier space without applying sophisticated compressed sensing-based methods or other regularization approaches. One of the possible solutions is to combine the information acquired in transmission and reflection [17–18]. However, if the backscattered information was additionally detected with two opposite reflection ODT systems, then the most complete spectrum coverage would be obtained – without even perturbing the sample with its rotation. One of the interesting solutions for this approach is to place the sample directly on the mirror and alter the illumination direction [19]. With this tool, the information backscattered is either collected directly by the system or through reflection off the mirror beneath the sample.

The one remaining strategy for data coverage increase in ODT is to use the fact that the diameter of the Ewald sphere is scaled with wavelength and thus, different

spheres may be mapped with a hyperspectral approach. Using multiple wavelengths is a desired modality since it can be used as another measure to characterize the sample [20] or to directly combine information from all wavelengths in the Fourier space [21]. In the second case the dispersion of the sample may be the source of reconstruction errors and, in general, should be compensated, especially if the wavelength range is significant for the sample measured. Accordingly, the wavelength scanning strategy may be used also in the case of reflective ODT and has been realized along with a vector-based approach to improve the axial resolution of the reconstruction result [22].

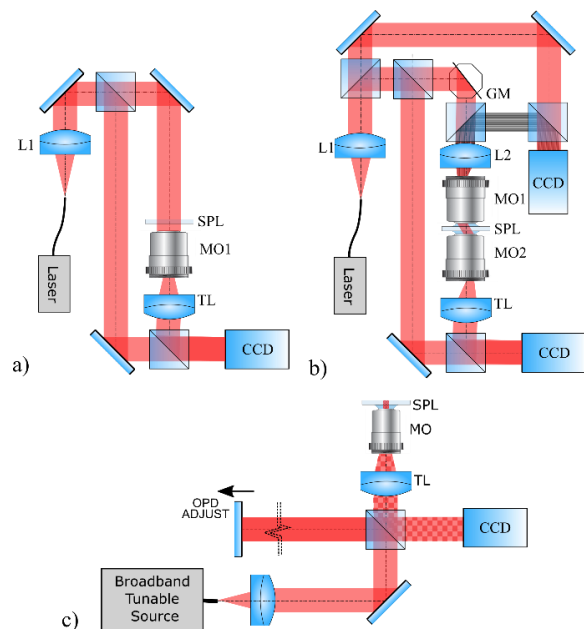


Fig. 2. Implementations of typical measurement systems for a) transmission digital holographic microscopy, b) dual-camera transmission and reflection mode optical diffraction tomography and c) Fourier domain full field optical coherence tomography. MO: microscope objective, SPL: sample plane, TL: tube lens, CCD: digital camera.

In this case, if only the wavelength scanning was to be performed at a constant illumination angle, the situation in the Fourier spectrum would be illustrated with Fig. 1d) and could be referred to as wavelength-scanning digital holography, but in fact the same spectrum coverage would be provided through Fourier domain full field optical coherence tomography (FD-FF-OCT) [6, 23]. A simplified idea of FD-FF-OCT realized with a swept-source is presented in Fig 2c.

Despite numerous implementations, all the OCT systems may be described with a unified K-space theory [6], which in this context could be also called Fourier diffraction theorem. The example of FD-FF-OCT presented in this paper is the closest implementation to DHM and ODT due to the usage of multiple wavelengths, and also one of the most dynamically developed implementations in recent years [24].

While the development of OCT was mostly based on a different theoretical model [6], it followed a direction towards quantitative phase imaging (QPI), which is a more general group of methods that includes DHM and ODT as the techniques capable of delivering reliable phase-based measurements. A few methods were developed in this pursuit, e.g. the FD-FF-OCT method was applied in transmission to retrieve the phase of the measured samples [25]. One of the interesting approaches was implementing the off-axis configuration in parallel FD-FF-OCT [26]. This solution, however, required axial scanning of the sample to perform tomography. Moving the sample – actually rotating to two angular positions was also used to assess the refractive index of the sample in FD-FF-OCT based on differences in the optical path length (sensitive to reconstruction misalignment) [27]. The method based on comparing optical path lengths of the sample to retrieve the refractive index of a layer was also possible without rotating the sample, but not without additional measurement modality – in this case OCT was supplemented with multiphoton microscopy, which unfortunately requires staining to retrieve second optical path length [28].

Recently, an interesting approach, which leans on traditional tomographic methods, has been proposed to solve the aforementioned lack of quantitative information [29]. The sample was rotated and at consecutive angular positions measured with OCT. The data was processed with a filtered back-projection algorithm and a forward model was used to optimize the 3D refractive index distribution and so far this has been the most advanced and successful proposition.

Both ODT and OCT are developed in the directions that head towards each other – ODT working in reflection mode to improve practical applicability and OCT

modified to provide quantitative information or two techniques merged together [18] that would provide new diagnostic tools in biomedicine. With a common ground – unified K-space theory we expect a multitude of new exciting systems to appear in the next few years.

Authors would like to acknowledge “BiOpTo: Tomographic phase microscope for biomedical applications” (POIR.04.04.00-00-1C1D/16-00) project carried out within the TEAM TECH programme of the Foundation for Polish Science co-financed by the European Union under the European Regional Development Fund.

References

- [1] N. Leith, J. Upatnieks, *J. Opt. Soc. Am.* **52**(10), 1123 (1962).
- [2] Y. Park, C. Depeursinge, G. Popescu, *Nat. Photonics* **12**, 578 (2018).
- [3] D. Huang *et al.*, *Science* **254**(5035), 1178 (1991).
- [4] D. P. Popescu, C. Flueraru, S. Chang, J. Disano, S. Sherif, M.G. Sowa, *Biophys. Rev.* **3**(3), 155 (2011).
- [5] M. Wojtkowski, V. Srinivasan, J.G. Fujimoto, T. Ko, J.S. Schuman, A. Kowalczyk, J.S. Duker, *Ophthalmology* **112**(10), 1734 (2005).
- [6] K.C. Zhou, R. Qian, A.-H. Dhalla, S. Farsiu, J.A. Izatt, *Adv. Opt. Photon.* **13**(2), 462 (2021).
- [7] A.F. Fercher, C.K. Hitzenberger, G. Kamp, S.Y. El-Zaiat, *Opt. Comm.* **117**(1-2), 43 (1995).
- [8] E. Wolf, *J. Opt. Soc. Am.* **60**(1), 18 (1970).
- [9] E. Wolf, *Opt. Comm.* **1**(4), 153 (1969).
- [10] V. Balasubramani *et al.*, *J. Imaging* **7**(12), 252 (2021).
- [11] A. Kuś, W. Krauze, P.L. Makowski, M. Kujawińska, *ETRI J.* **41**(1), 61 (2019).
- [12] A. Kuś, M. Dudek, M. Kujawińska, B. Kemper, A. Vollmer, J. Biomed. Opt. **19**(4), 46009 (2014).
- [13] O. Haeberlé, K. Belkebir, H. Giovaninni, A. Sentenac, *J. Mod. Opt.* **57**(9), 686 (2010).
- [14] B. Simon *et al.*, *Optica* **4**(4), 460 (2017).
- [15] B.A. Roberts, A.C. Kak, *Ultrason. Imag.* **7**, 300 (1985).
- [16] M. Sarmis *et al.*, *J. Mod. Opt.* **57**(9), 740 (2010).
- [17] L. Foucault *et al.*, *J. Opt. Soc. Am. A* **36**(11), C18 (2019).
- [18] W. Krauze, P. Ossowski, M. Nowakowski, M. Szkulmowski, M. Kujawińska, *Proc. SPIE* **11653**, 116530B (2021).
- [19] E. Mudry, P.C. Chaumet, K. Belkebir, G. Maire, A. Sentenac, *Opt. Lett.* **35**(11), 1857 (2010).
- [20] P. Hosseini, Y. Sung, Y. Choi, N. Lue, Z. Yaqoob, P. So, *Opt. Expr.* **23**(15), 19752 (2015).
- [21] J. Jung, K. Kim, J. Yoon, Y. Park, *Opt. Expr.* **24**(3), 1881 (2016).
- [22] T. Zhang *et al.*, *Biomed. Opt. Expr.* **26**(20), 26093 (2018).
- [23] R.A. Leitgeb, *Biomed. Opt. Expr.* **10**(5), 2177 (2019).
- [24] J.F. de Boer, R. Leitgeb, M. Wojtkowski, *Biomed. Opt. Expr.* **8**(7), 3248 (2017).
- [25] T. Anna, V. Srivastava, C. Shakher, *IEEE Photon. Technol. Lett.* **23**(11), 899 (2011).
- [26] M.T. Rinehart, V. Jaedicke, A. Wax, *Opt. Lett.* **39**(7), 1996 (2014).
- [27] C. Photiou, C. Pitris, *J. Biomed. Opt.* **24**(10), 1 (2019).
- [28] Y. Zhou, K.K.H. Chan, T. Lai, S. Tang, *Biomed. Opt. Expr.* **4**(1), 38 (2013).
- [29] K.C. Zhou, R. Qian, S. Degan, S. Farsiu, J.A. Izatt, *Nat. Photon.* **13**, 794 (2019).

Optical properties of antimony-borate glass rods co-doped with $\text{Eu}^{3+}/\text{Ag}^+$ ions

Karol Czajkowski,*¹ Magdalena Leśniak,² Marcin Kochanowicz,¹ and Jacek Zmojda¹

¹Faculty of Electrical Engineering, Białystok University of Technology, 45d Wiejska St. 15-351 Białystok,

²Faculty of Materials Science and Ceramics, AGH University of Science and Technology, 30 Mickiewicza St., 00-667 Krakow.

Received October 12, 2021; accepted December 02, 2021; published December 31, 2021

Abstract—This paper presents the results of research on the luminescent properties of antimony-borate glass rods doped with europium and silver ions. The reduction of silver ions to a form of nanoparticles was carried out and the occurrence of localized plasmon resonance was demonstrated, which caused changes in the Eu^{3+} luminescence signal at a wavelength of 613 nm. The effect of the concentration of silver ions dopant at a constant content of europium ions on the luminescence and absorption characteristics of the produced samples was investigated. In the examined doping range, no large dependencies of spectral changes as a function of silver ions concentration were found. Clear quenching of luminescence was observed due to the heating time of doped glass matrices for energy transition ($^5\text{D}_0 \rightarrow ^7\text{F}_2$).

The technology of nanocomposite glasses containing noble metal nanoparticles is widely researched due to the possibility of overcoming typical limitations of fused quartz (for instance, bandwidth, luminescence efficiency, and nonlinearity) and high application potential. Optical fibers based on this technology combine both the mechanical and chemical properties of a glass matrix with extended spectroscopic properties of embed metal nanoparticles (NPs) [1–4]. Therefore, in the technological process of glass synthesis, in addition to active doping (rare earth elements), noble metal ions are introduced into the structure, and then, as a result of controlled thermal treatment, metallic NPs are formed. As a result of collective oscillations of free electrons, plasmons are formed on the surface of metal nanoparticles. Such a phenomenon is referred to as localized surface plasmon resonance (LSPR) [6]. The effect of the surface plasmon resonance depends on the type of material, shape and dimension of NPs, as well as dielectric features and index of refraction. Therefore, the change of geometry (rods, sphere) of metallic nanoparticles and the physicochemical properties of the host, in which it is located, leads to changes in the interaction of metallic nanoparticles with optical radiation resulting from the plasmon localized on the surface of metallic nanoparticles. In the literature, there are many studies on obtaining localized surface plasmon resonance in many glasses, including antimony [5], tellurium [6], phosphate [7] or lead-germanium [9].

Sb_2O_3 has a chemical potential that allows the reduction of silver ions directly in the process of thermochemical synthesis. The heating process, in which nanoparticles are formed at a temperature above glass transformation, increases the concentration of nanoparticles in the glass structure. According to the energy structure of europium ions it is possible to obtain a plasmonic effect and energy transfer between Ag NPs and Eu^{3+} ions, which allow the enhancement or quenching of the luminescence. This mechanism is strongly depended on the concentration of Ag NPs and the heating time. Also, Schneider *et al.*, report non-conventional silver nanoparticle growth on the surface of lead-germanate oxide glasses which can be used as an active layer in plasmonic sensors [9]. The article presents research on obtaining the plasmonic effect in glass rods with different content of silver ions and heating time. The produced glass rods were doped with Eu^{3+} ions whose excited-state absorption band harmonizes with the plasmon band of silver nanoparticles. Moreover, as a result of heating, a surface reduction of silver ions was observed, which can be used as active layers in optoelectronic sensors.

Antimony-borate glass rods were made from glass composition [%mol]: $25\text{Sb}_2\text{O}_3\text{-}25\text{GeO}_2\text{-}45\text{B}_2\text{O}_3\text{-}5\text{Na}_2\text{O} - x\text{AgNO}_3 - 0.5\text{Eu}_2\text{O}_3$, where $x = 0.5; 1; 1.5$. The homogenized sets were melted in a platinum crucible at 1450°C . Next, the glass was cast in a brass mold and annealed in a furnace at 380°C for 12 hours. The preform prepared in this way was processed into glass rods with a diameter of 1 mm and length of 100 mm (Fig. 1). The observed brown color of (c) rod stems from partial reduction of nanoparticles during thermal drawing. Measurements of optical properties in the visible range were carried out by using a Stelarnet GreenWave optical spectrometer and a laser diode emitting at a wavelength of 395 nm. Surface changes were recorded using electron scanning microscopy SEM.

Figure 2 shows the luminescence spectra of antimony-borate glass rods doped with 0.5 mol.% Eu_2O_3 and with a different content of silver ions, obtained with excitation of

* E-mail: czajkowski.karoll@gmail.com

395 nm laser radiation. The europium ion luminescence bands in the visible range at the wavelengths of 570 nm, 590 nm, 613 nm, 660 nm and 700 nm are assigned to the corresponding radial transitions from the 5D_0 level to the baseline levels 7F_0 , 7F_1 , 7F_2 , 7F_3 , 7F_4 , respectively.

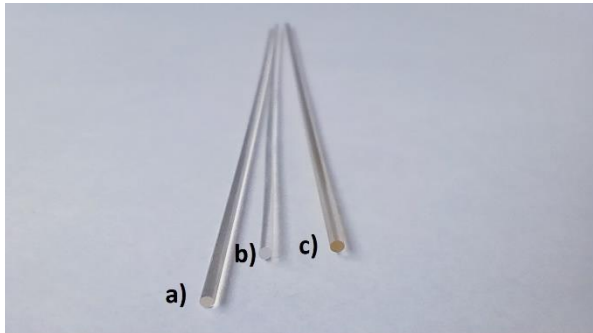


Fig. 1. Fabricated glass rods of antimony-borate glasses (a) SGBNa_1.0Ag_0.5Eu, (b) SGBNa_0.5Ag_0.5Eu, (c) SGBNa_1.5Ag_0.5Eu.

Established on the spectral analysis of the produced glass rods, it was observed that an increase in the concentration of silver causes a slight decrease in the level of luminescence. It is strictly related to the partial reduction of silver ions to the form of nanoparticles in the rod forming process, which was confirmed by absorption measurements (Fig. 3). It is clearly visible that the absorption band with the maximum at a wavelength of 460 nm grows with the increase in the concentration of silver ions. The appearance of the plasmon band also confirms the obtaining of silver nanoparticles in the antimony-borate glass.

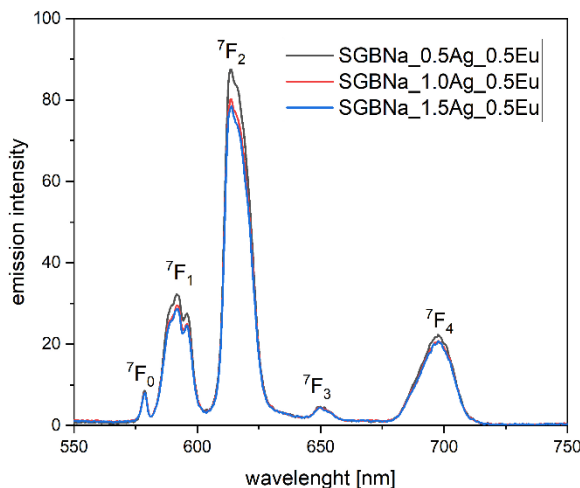


Fig. 2. Luminescence spectrum of SGB glass rods co-doped with $0.5\text{Eu}_2\text{O}_3$ and three concentrations of Ag ions.

Due to the strong quenching of the luminescence signal, glass rods doped with 0.5 mol% AgNO_3 were selected in the next stage of the study, which was heated at the temperature of 400°C for 60 minutes (heating in a furnace for 15 minutes, then taking measurements, and again in the

same order for a total of 60 minutes). The Figure indicates analogous luminescence spectra obtained when the rods are excited with laser radiation at a wavelength of 395 nm. As it can be seen, additional heating of the produced rods causes an increase of luminescence after 15 min which suggests that a plasmon effect occurred. For longer heating time the intensity decrease, which is related to the undesirable energy back-transfer between europium ions and silver nanoparticles.

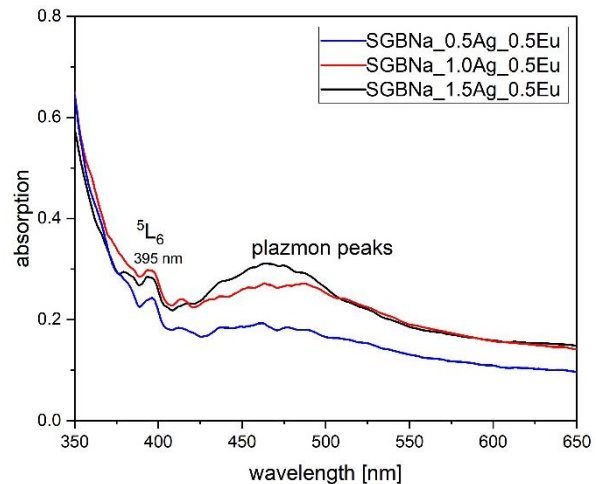


Fig. 3. Absorption spectrum of SGB glass rods doped with $0.5\text{Eu}_2\text{O}_3$ and three concentrations of Ag ions.

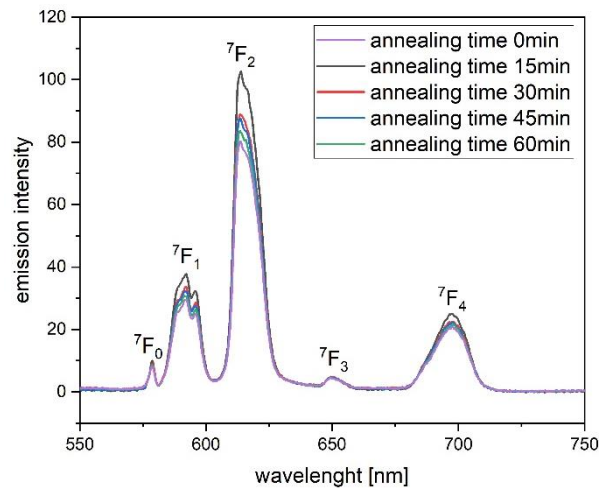


Fig. 4. Luminescence spectrum of SGBNa_0.5Ag_0.5Eu glass rod in relation to the annealing time.

What is more, the most visible changes take place at a wavelength of 612 nm (Fig. 4), corresponding to the energy transition from $^5D_0 \rightarrow ^7F_2$. Based on the observation of the annealed rods, it was determined that the decrease in luminescence is caused by the growth of nanoparticle structures and the formation of conglomerates on the material surface. As a result, small rods changed their color. While examining the absorption spectra for the SGB_0.5Eu_0.5Ag rod, it was observed that the absorption

band corresponding to the plasmon vibration increased for the first 45 minutes and then remained constant.

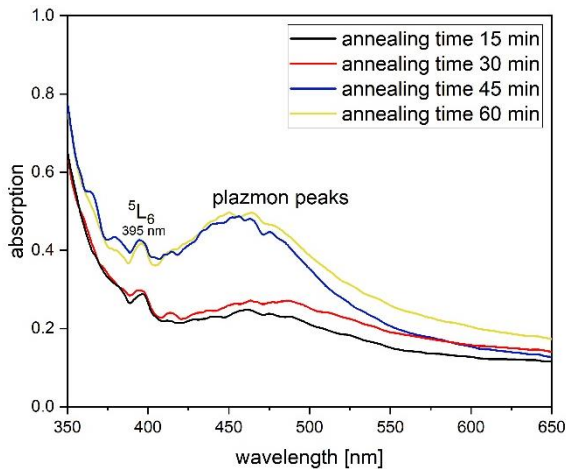


Fig. 5. Absorption spectrum of SGB_0.5Ag_0.5Eu glass rod in relation to the annealing time.

The observed phenomenon was described by the Schneider *et al.*, where, as a result of the migration of silver ions, their self-organization took place on the surface of lead-germanium glasses [9]. Heating time favors the formation of continuous metallic layers on the glass surface and thus the local electric field decreases and, consequently, the level of luminescence decreases. In order to confirm the plasmonic effect and surface reduction of silver ions, surface morphology studies were performed using electron scanning microscopy (SEM). Figure 6 shows photographs that were taken for the surface of the SGBNa_0.5Ag_0.5Eu rod immediately after production and after additional one-hour heating at 400°C. The scale of measurement was the same, hence easy comparison of the size on nanoparticles was made.

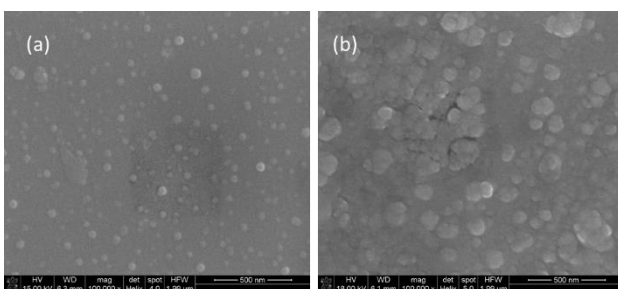


Fig. 6. SEM photo of the surface of glass rod SGB_0.5Ag_0.5Eu a) after fabrication, b) after annealing.

Based on the measurements and EDS analysis, it was found that spherical silver nanoparticles were formed on the surface of the produced antimony-borate rods. Their arrangement is relatively homogeneous, which confirms the stability of used technology. In the parent glass rod the particle size was estimated approx. at 60 nm (Fig. 6a) and after the annealing process (Fig. 6b) the NPs size increased

up to 130 nm. Also, it is worth noticing that the warming-up process leads to the accumulation of nanoparticles. Their large increase was caused by their being pushed to the upper glass layer and a significant increase in their size compared to the initial size.

In summary, in the article we present research on the optical properties of antimony-borate rods doped with Eu ions and various concentrations of silver ions. Antimony glasses are characterized by high thermal stability, which is a promising matrix for the production of optical fibres with suspended metallic nanoparticles. In the absorption spectrum, characteristic plasmon peaks for the wavelength of 460 nm originating from silver ions were observed. The phenomenon of luminescence quenching indicated the migration of energy from europium ions to silver ions, which depends on the larger volume fraction, and as a result of heating a larger size of silver nanoparticles formed. The highest dependence of luminescence suppression due to warming up was observed for the wavelength of 613 nm. Furthermore, as a result of heating the developed antimony-borate rods, the ability of self-organization of nanoparticles on the material surface was demonstrated.

The project was funded by National Science Centre (Poland) granted on the basis of the decision No. DEC-2016/21/D/ST7/03453 and partially by Bialystok University of Technology from grant No. WZ/WE-IA/3/2020.

References

- [1] S. Kuzman, J. Perisa, V. Dordevic, I. Zekovic, I. Vukoje, Z. Antic, M.D. Dramicanin, *Materials* **13**, 3071 (2020).
- [2] V.P. Prakashan, M.S. Sajna, G. Gejo, M.S. Sanu, A.C. Saritha, P.R. Biju, J. Cyriac, N.V. Unnikrishan, *Plasmonics* **14**, 673 (2019).
- [3] O. Malta, P. Santa-Cruz, G. Sa, F. Auzel, *J. Lumin.*, **33**, 261 (1985).
- [4] O. Malta, P. Santa-Cruz, G. Sa, F. Auzel, *Chem. Phys. Lett.*, **116**, 396 (1985).
- [5] J. Zmojdza, M. Kochanowicz, P. Miluski *et al.*, *J. Mol. Structure* **1160**, 428 (2018).
- [6] K.Y. Kim, *Plasmonics: Principles and Applications* (Croatia, InTechOpen 2012).
- [7] M.R. Dousti, M.R. Sahar, S.K. Ghoshal *et al.*, *J. Non-Crystalline Solids* **358**, 2939 (2012).
- [8] I. Soltani, S. Hraiech, K. Horchani-Naifer *et al.*, *Opt. Materials* **46**, 454 (2015).
- [9] R. Schneider, E.A. de Campos, J.B.S. Mendes, J.F. Felix, P.A. Santa-Cruz, *RSC Advances* **7**(66), 41479 (2017).